







RESEARCH ARTICLE

Sensitivity of some African heavy rainfall events to microphysics and planetary boundary layer schemes: Impacts on localised storms

Agostino N. Meroni^{1,2}  | Kizito A. Oundo³ | Richard Muita³ |
Mary-Jane Bopape⁴  | Thizwilondi R. Maisha⁴  | Martina Lagasio²  |
Antonio Parodi²  | Giovanna Venuti¹ 

¹Department of Civil and Environmental Engineering, Politecnico di Milano, Milan, Italy

²CIMA Research Foundation, Savona, Italy

³Kenyan Meteorological Department, Nairobi, Kenya

⁴South African Weather Service, Centurion, South Africa

Correspondence

A. N. Meroni and G. Venuti, Department of Civil and Environmental Engineering, Politecnico di Milano, Milan 20133, Italy, E-mail: agostino.meroni@gmail.com; giovanna.venuti@polimi.it

Funding information

European Union's Horizon 2020 Research and Innovation Programme, Grant/Award Number: 776691

Abstract

High-resolution numerical weather prediction (NWP) simulations of heavy rainfall events are known to be strongly sensitive to the choice of the sub-grid scale parameterisation schemes. In the African continent, studies on such a choice at the convective-resolving scales are not numerous. By exploiting a state-of-the-art NWP model, the Weather Research and Forecasting (WRF) model, the sensitivity of the simulation of three heavy rainfall events in Sub-Saharan Africa to the microphysical (MP) and planetary boundary layer (PBL) schemes is studied. Validating the numerical outputs against rainfall satellite estimates, ground-based weather stations, radiosonde profiles and satellite-derived cloud-top temperature maps with an object-based tool, the best-performing setup is identified. In terms of heavy rainfall forecast location, it is found that the PBL scheme has a greater impact than the MP, which is shown to control the cloud-top temperature simulation. Among the schemes considered, the best performances are achieved with a six-class single-moment microphysical scheme and a non-local planetary boundary layer scheme which properly includes the vertical mixing by the large eddies in the atmosphere.

KEYWORDS

Africa, heavy rainfall, microphysics, MODE, NWP model, planetary boundary layer, WRF

1 | INTRODUCTION

High-resolution numerical simulations of heavy rainfall are necessary to better understand the small-scale and complex dynamics of the atmosphere that leads to high-impact weather events (Roberts *et al.*, 2018, HIWEs).

These events strongly affect society and are not easy to forecast, especially with global numerical weather prediction (NWP) models (Vogel *et al.*, 2018). The low skills in predicting HIWEs are generally ascribed to small-scale processes that low-resolution models cannot capture explicitly and have to be approximated statistically or

parameterised. These parameterisation schemes are associated with most of the uncertainty in model simulations. In particular, the convection parameterisation schemes have a significant influence on heavy rainfall phenomena, because they unavoidably represent some important factors for rainfall development (such as temperature and humidity vertical distribution, vertical motion, amongst others) in a crude way (e.g., Maranan *et al.*, 2018).

Regional NWP models perform better than global models in simulating such events, thanks to their finer spatial resolution, especially when convection is explicitly resolved with grid lengths of less than 4–5 km. Regional models run with high resolution over the area of interest and, thus, can produce more detailed simulations than is possible with global models using the same amount of computational resources. An example of a sensitivity study in Africa on climatic time scales is the work of Cr  tat *et al.* (2014), which demonstrates the added value of regional climate modelling with respect to general circulation models, in particular concerning the dynamics that lead to heavy rainfall events. Other examples of efforts to properly simulate the African climate are the numerical works pursued within the COordinated Regional climate Downscaling EXperiment (CORDEX) framework (e.g., Laprise *et al.*, 2013). The increased computer power that has become available in recent years has opened up the possibility to explore the dynamical evolution of HIWEs in an unprecedented way. However, most of the research in the African continent has been performed on climatic and seasonal time scales, with very few studies of high-resolution simulations of HIWEs.

The Weather Research and Forecasting (WRF) model (Skamarock *et al.*, 2019) is a state-of-the-art, fully compressible atmospheric model that is used for both research and operational applications, over a wide range of spatio-temporal scales. In the literature, many studies have focused on the sensitivity of WRF-simulated rainfall predictions to various physical schemes over relatively long time scales, including seasons, years and decades. A non-exhaustive list of these works for Eastern, Western and Southern Africa is discussed below. Table 1 contains the full name of the WRF physics schemes mentioned in what follows, together with their bibliographic references.

East Africa is on the boundary between the West African and the Indian monsoons. Its rainfall regime is characterised by the convective activity of the Inter-Tropical Convergence Zone (ITCZ), strongly modulated by local factors (Nicholson, 2017). Pohl *et al.* (2011) study the sensitivity of the East African regional climate with respect to some WRF physical parameterisations. In particular, they consider convection (CU), microphysics (MP), planetary boundary layer (PBL), land surface model (LSM) and radiation schemes (RAD), as well as changes in

the land-use categories at the seasonal scale. Their simulations are conducted with a grid spacing of 36 and 12 km, and they find that, in order of importance, the simulations are most sensitive to the short-wave RAD, the LSM, the domain size, the CU and the land-use categories. Cloud MP, lateral forcing reanalysis, the number of vertical levels and PBL schemes appear to be less important. The fact that the CU does not significantly modify the rainfall pattern on seasonal time scales is also confirmed by Otieno *et al.* (2020), who investigate the sensitivity of the WRF model seasonal rainfall simulations in East Africa to four CU schemes, namely KF, KFT, GRELL and BMJ. They find that all the CU schemes considered are able to reproduce the large-scale rainfall distribution, with different biases due to different physical approaches implemented in the schemes. In the same African region, Sun *et al.* (2015) focus their attention on the dependence of the simulated spatial rainfall pattern on the lake surface temperature of Lake Victoria, which is known to play a significant role in the regional climate. Running 5-day simulations with 12- and 4-km horizontal resolution, with some sensitivity study that they do not show, they identify the optimal set of physical parameterisations as: RRTM for longwave RAD, Dudhia for shortwave RAD, UNOAH LSM, ETA MP, GRELL CU and ACM2 for the PBL, with the MM5 similarity surface layer (SL) scheme.

Regarding West Africa, several studies compare the model output with various observational datasets, with the majority of the studies focusing on seasonal or longer time scales, and corresponding coarse spatial resolutions. Noble *et al.* (2014; 2017) investigate the sensitivity of WRF model simulations to numerous physical schemes (namely PBL, CU, LSM and RAD) using a horizontal grid spacing of 20 km, over 12 days of simulation. The GRELL scheme is found to be the best choice for the CU parameterisation in this region. By validating the simulations with the vorticity field (Noble *et al.*, 2014), the RRTM RAD scheme appears to perform well, while the Noah LSM and the MYNN PBL scheme are found to be less skilful. By validating the same simulations with respect to the rainfall field (Noble *et al.*, 2017), the Noah LSM appears again to perform poorly with respect to the RUC and the PX LSMs. The overall best configuration is composed of the following schemes: GRELL, RUC, ACM2 and RRTM. Also, Meynadier *et al.* (2015) perform some sensitivity study in West Africa using a grid spacing of 25 km, with a focus on air–sea interactions. They find that the PBL strongly influences the wind response to the SST and the water cycle, with the non-local schemes obtaining the best results with respect to radiosonde data. They also find that the rainfall spatial distribution is mostly affected by the RAD scheme and the MP scheme has a significant impact on the radiation heating profiles and the resulting precipitation. For the

TABLE 1 WRF physics schemes mentioned in the main text with their acronyms and references

MP: Microphysics		
	- WRF Single Moment 6-class (WSM6)	Hong and Lim (2006)
	- Thompson (THOM)	Thompson <i>et al.</i> (2008)
	- Eta (ETA)	NOAA (2001)
	- Morrison (MORR)	Morrison <i>et al.</i> (2009)
	- New Thompson (NTHOM)	Thompson and Eidhammer (2014)
PBL: Planetary boundary layer	- Yonsei University (YSU)	Hong <i>et al.</i> (2006)
	- Mellor–Yamada–Janjic (MYJ)	Janjic (1994)
	- Asymmetric Convection Model 2 (ACM2)	Pleim (2007)
	- Mellor–Yamada–Nakanishi–Niino (MYNN)	Nakanishi and Niino (2006)
CU: Cumulus		
	- Kain–Fritsch (KF)	Kain (2004)
	- modified Kain–Fritsch (KFT)	Ma and Tan (2009)
	- Grell–Dévényi (GRELL)	Grell and Dévényi (2002)
	- Betts–Miller–Janjic (BMJ)	Janjic (1994)
	- New Tiedtke (NTD)	Zhang and Wang (2017)
RAD: Radiation	- Rapid Radiative Transfer Model (RRTM) (longwave)	Mlawer <i>et al.</i> (1997)
	- RRTM for Global Circulation Models (RRTMG)	Iacono <i>et al.</i> (2008)
	- Dudhia (shortwave)	Dudhia (1989)
LSM: Land surface model		
	- Rapid Update Cycle (RUC)	Benjamin <i>et al.</i> (2004)
	- Unified Noah (UNOAH)	Chen and Dudhia (2001)
	- Pleim–Xiu (PX)	Gilliam and Pleim (2010, and refs therein)
SL: Surface layer	- Revised MM5 similarity (RMM5)	Jiménez <i>et al.</i> (2012)
	- Eta similarity (ETAS)	Janjic (1994)

Note: The schemes evaluated in the present work are highlighted in bold font.

radiation scheme, RRTMG is found to give the best results, and for the MP the MORR parameterisation (which is a two-moment scheme) is found not to work properly. Kouadio *et al.* (2018) run numerical simulations at a grid spacing of 24 and 4 km to assess the benefit of explicitly resolving convection in monthly or seasonal simulations of the West African Monsoon (WAM) season of 2014. They study the sensitivity of the WRF model to MP (using WSM6, MORR and NTHOM) and PBL (MYJ, YSU and ACM2) schemes and discover that the PBL has a stronger impact on rainfall distribution. In particular, configurations using

non-local PBL schemes (such as ACM2) outperform the others, especially when convection is parameterised.

In the southern part of the continent, Crétat *et al.* (2012) study the sensitivity of the WRF austral summer simulations to CU, PBL and MP schemes using a grid spacing of 35 km and validating the experiments with ground-based sensors. Their results indicate that the seasonal rainfall amount is the most sensitive variable to the schemes under study, with CU having the greatest effects. Despite finding that the biases of different schemes roughly sum up and, thus, oppositely biased schemes can

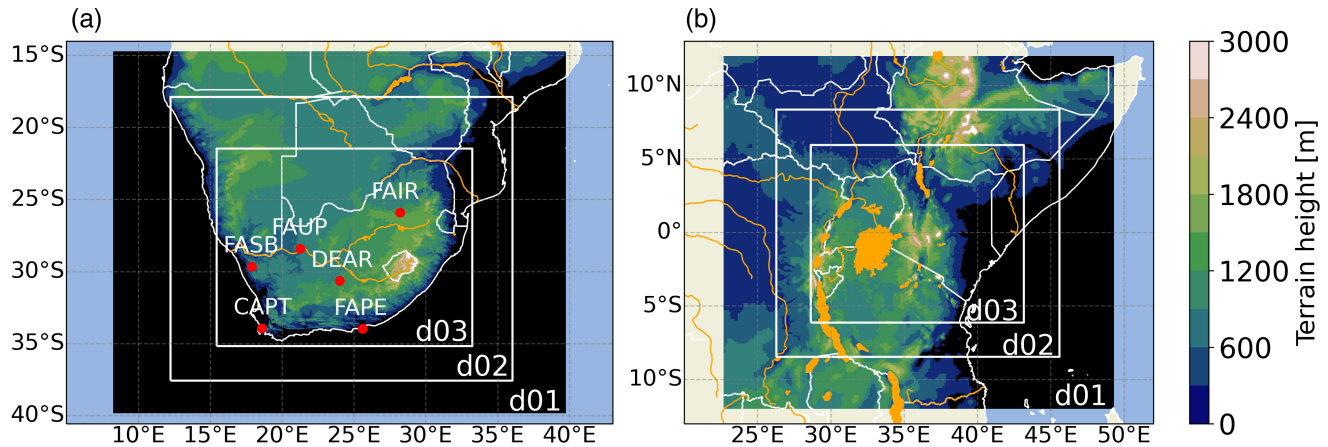


FIGURE 1 Domain set-up of the two regions under study, namely (a) South Africa, and (b) Kenya–Uganda, showing the model orography in colour shading, the country borders as white lines and the major rivers and lakes in orange. In (a) the red dots denote the position of the available radiosonde stations. The horizontal grid spacing of the three domains (white boxes) is 13.5, 4.5 and 1.5 km, respectively [Colour figure can be viewed at wileyonlinelibrary.com]

balance out one another, they discourage the use of BMJ CU and MYJ PBL schemes for Southern African summer applications. Specifically, the MYJ PBL scheme is found to produce wet biases in the simulations. Keat *et al.* (2019) study the convective initiation during the austral summer using convection-resolving simulations. They find that the physical parameterisation schemes that make the dynamics smoother (e.g., stronger mixing or larger mixing length scales) tend to postpone the convective initiation. Moreover, they highlight that physical schemes can never compensate for errors in the initial and boundary conditions. Maisha (2014) study the role of topography and grid spacing on the simulation of extreme weather events that caused floods in South Africa. Using WRF numerical simulations at 9- and 3-km grid spacing, the GRELL CU scheme is found to over-predict the accumulated rainfall.

Schemes that work well on climatic scales do not automatically work well at event time scales. Thus, sensitivity studies are needed to tune the models for better HIWE forecasts. Numerical schemes can be optimised depending on the geographical location, the time of the year and the dynamics of the event, for example. Such high-resolution short numerical simulations are computationally expensive, but they provide more insight into the dynamics of HIWEs. In the framework of the Transforming Weather and Water data into value-added Information services for sustainable Growth in Africa (TWIGA) project, three representative HIWEs in Sub-Saharan Africa are studied. The goal of the present work is to evaluate the sensitivity of cloud-resolving WRF model simulations to some relevant MP and PBL schemes. In particular, one event in Eastern Africa and two events in Southern Africa are considered. Section 2 describes the model setup and the validation products. Section 3 introduces the case studies, followed

by the results in Section 4. Conclusions are drawn in Section 5.

2 | MODEL SETUP AND OBSERVATIONAL DATA

2.1 | Numerical model configuration

Three heavy rainfall events, described in the next section, are studied with convection-permitting numerical simulations run with the WRF model V4.0.3 (Skamarock *et al.*, 2019). The initial and 3-hourly boundary conditions are obtained from the European Centre for Medium-Range Weather Forecasts Integrated Forecasting System (ECMWF-IFS) forecast product at 0.125° horizontal grid spacing. Due to a mismatch between the land–sea masks of the WRF numerical grids and the ECMWF-IFS product, bubbles of very cold SST (near 0°C) are observed if the standard WRF Pre-processing System (WPS) tools are used. Thus, the original IFS-ECMWF land–sea mask is extended over the sea to remove such cold features before running the WPS (not shown). For each case study, three two-way nested domains are set up with 40 vertical levels and grid spacing of 13.5, 4.5 and 1.5 km, respectively (Figure 1). The innermost domain always covers a region larger than $1,300 \times 1,300$ km. Note that, due to computational power constraints, no sensitivity test on the number of vertical levels is performed in this study and is left for future work.

The physical schemes are chosen as informed by previous studies, as outlined in the “Introduction.” In particular, the starting point is the WRF tropical suite, which is the set of schemes suggested in the WRF model community

to properly work in tropical environments (Wang, 2017). This includes: WSM6 for the MP, NTD for CU, RRTMG for longwave and shortwave RAD, YSU for PBL, RMM5 for SL and UNOAH for LSM. The choice of RRTMG for the radiation scheme is confirmed by other studies, including Noble *et al.* (2014; 2017); Meynadier *et al.* (2015) and Kouadio *et al.* (2018). Concerning the LSM, the UNOAH model is often used (Meynadier *et al.*, 2015; Sun *et al.*, 2015; Kouadio *et al.*, 2018). However, Noble *et al.* (2014; 2017) find that, among the numerous numerical scheme combinations that they test, the RUC model characterises most of the best-performing configurations they identify in terms of daily rainfall and circulation, which is why we choose it here. Given that the current experiments aim to test the sensitivity of a convection-permitting setup to the PBL schemes and the MP schemes, the following PBL and MP choices are selected: YSU, MYJ and ACM2 for PBL, and WSM6 and THOM for MP.

The most relevant features of the selected PBL schemes are the following. YSU (Hong *et al.*, 2006) is a non-local PBL scheme with a counter-gradient term in the turbulence diffusion equation to represent the mixing produced by large eddies. It also includes an explicit term that represents the mixing at the top of the boundary layer due to entrainment processes. MYJ (Janjic, 1994) is a local PBL scheme based on the Mellor–Yamada level 2.5 turbulence closure equations, originally developed for the step-mountain eta coordinate model. It is coupled with a surface layer scheme based on a Mellor–Yamada level 2 turbulence closure. ACM2 (Pleim, 2007) is a non-local scheme that represents the vertical mixing induced by large eddies with a transilient asymmetric matrix approach (to distinguish between upward and downward mass transport) and represents the sub-grid-scale mixing with a standard diffusive term. It is worth noticing that, with respect to counter-gradient models such as YSU, the transilient matrix approach makes ACM2 more effective in describing the vertical transport of quantities other than temperature (e.g., humidity, winds or trace chemical mixing ratios). Concerning the MP schemes under study, the WSM6 parameterisation (Hong and Lim, 2006) is a single-moment scheme, meaning that it only solves the equations for the mixing ratios, and considers five microphysical species: cloud, rain, ice, snow and graupel. It represents the snow and graupel mixed-phase particle terminal velocity by weighting their separate terminal velocities with their mixing ratio. The THOM scheme (Thompson *et al.*, 2008) considers the same five microphysical species, but has a double-moment approach for cloud water, ice and rain. This means that, for these three hydrometeors, it also solves the equations for the number concentration variables. With respect to its previous

TABLE 2 Starting and end UTC dates of the numerical experiments

Case study	Starting date	End date
KU_May2018	May 19, 2018 00:00:00	May 23, 2018 00:00:00
SA_Jan2017	January 4, 2017 00:00:00	January 8, 2017 00:00:00
SA_Mar2018	March 21, 2018 00:00:00	March 24, 2018 00:00:00

versions, it includes more refined spectral bin schemes that exploit updated look-up tables.

Note that the choice of the SL scheme is sometimes tied to the PBL one. In particular, when using YSU and ACM2 PBL schemes, the RMM5 is selected as SL, while when using MYJ PBL, the ETAS SL (a Mellor–Yamada level 2 turbulence closure) is activated. The names of the experiments contain the MP and PBL schemes selected, as described in Section 3. Table 2 indicates the starting and end UTC dates for all the experiments of the three case studies.

2.2 | Observational data sets

Concerning the validation data sets, both ground-based sensors and satellite rainfall estimates are used. For Kenya and Uganda, observations come from the Kenyan Meteorological Department (KMD) network (in Kenya) and the Trans-African Hydro-Meteorological Observatory (van de Giesen *et al.*, 2014, TAHMO) network (in both countries), while for South Africa the automatic weather stations (AWSs) and the automatic rainfall stations (ARSSs) from the South African Weather Service (SAWS) are available.

Despite the ongoing efforts of the TAHMO project to install 20,000 low-cost weather stations in the entire African continent and the working stations managed by meteorological centres, the available ground-based stations are still sparse. For this reason, satellite estimates are used to quantitatively validate the rainfall simulations. Two products that have been shown to perform well in Sub-Saharan Africa for event-based studies, according to Le Coz and van de Giesen (2020), are considered: the Integrated Multi-satellite Retrievals for GPM (Global Precipitation Measurement) or IMERG product (Huffman *et al.*, 2019), and the CPC (Climate Prediction Center) Morphing technique or CMORPH product (Joyce *et al.*, 2004). Both products have 30-min temporal sampling. The IMERG Final product is given on a regular 0.1° grid, while CMORPH is on a 0.07277° grid (8 km at the Equator).

While the IMERG Final product is based on a blending between microwave and infrared rainfall observations, calibrated with rain gauges on a monthly basis, CMORPH is a microwave-only product. More details on the description of the two satellite products, their algorithms and a cross comparison of their performances in Sub-Saharan Africa are available in the recent review paper by Le Coz and van de Giesen (2020).

Examples of studies that validate the performance of the IMERG rainfall estimates over Africa are Dezfuli *et al.* (2017a; 2017b). Dezfuli *et al.* (2017b) compare some rainfall events in East and West Africa using TAHMO weather stations and IMERG. They find good statistical agreement between the two data sets, highlighting IMERG's better performances with respect to its predecessor, the TRMM (Tropical Rainfall Measuring Mission) Multisatellite Precipitation Analysis (Huffman *et al.*, 02 2007, TMPA). Dezfuli *et al.* (2017a) carry out a systematic validation of IMERG over the African continent and find that IMERG captures the rainfall diurnal cycle better than TMPA (especially in Eastern and Southern West Africa) and has a reduced bias over Lake Victoria.

Radiosonde data are available for the South African case study through the University of Wyoming website (<http://weather.uwyo.edu/upperair/sounding.html>). During the events under study, observations from the stations in Cape Town (CAPT), Port Elizabeth (FAPE), Upington (FAUP), Springbok (FASB), Pretoria (FAIR) and De Aar (DEAR) are considered (see the left panel of Figure 1 for their locations).

Daily averages of cloud-top temperature (CTT) data measured by the Spinning Enhanced Visible and Infrared Imager (SEVIRI) instrument on board the METEOSAT second-generation spacecraft are also used to validate the simulations. These products are given at 0.05° grid spacing, and their references are Finkensieper *et al.* (2020) for the South African January 2017 case study and Finkensieper *et al.* (2018) for the 2018 case studies. They are available from the Climate Monitoring Satellite Application Facility (CM SAF) platform (https://www.cmsaf.eu/EN/Home/home_node.html, accessed August 2020).

3 | CASE STUDIES

The three events under study are selected because they caused serious damage in some of the regions of interest of the TWIGA project and because they are representative HIWEs in the regions under study. In particular, here, the synoptic conditions leading to the events are described, together with the corresponding regional climate framework.

3.1 | Kenya–Uganda

Eastern Africa rainfall annual variability is characterised by a bi-modal rainfall regime, which is generally interpreted as a direct consequence of the meridional displacement of the ITCZ (Camberlin and Philippon, 2002). The findings of Nicholson (2018), to cite one example, challenge this paradigm, highlighting the importance of local factors (e.g., orography, secondary circulations, land–sea thermal contrasts) in modulating the regional climate. For example, the Turkana Jet is characteristic of the local circulation and has been shown to be important in the regulation of the rainfall seasonality (Nicholson, 2016). It is named after Turkana Lake (in north-western Kenya) and it blows at 900–850 hPa from south-east to north-west, channelled by the relatively low topographic features of the Great Rift Valley between 35–40° E and 0–5° N. Its annual dynamics is linked to the formation of a convergence area over the Kenya–Uganda border during the so-called long rainy season (March–April–May, MAM). Such a convergence zone has been shown to be responsible for a high amount of accumulated rainfall in this area (Nicholson, 2016).

Despite being a single rainy season, Nicholson (2017) underlines that the dynamics that controls the May rainfall regime is not the same as in March and April. In particular, in May, the approaching onset of the Indian monsoon is found to be strongly correlated with the end of the rainy season, showing that the May rainfall regime is controlled by large-scale dynamics involved in the Indian monsoon development (Camberlin *et al.*, 2010). Moreover, MAM rainfall cessation corresponds to the northward shift of the peak solar forcing, such that the warmer regime migrates northward. This is accompanied by a stronger control of the weather conditions in East Africa by the Mascarene High (a high-pressure system in the southern Indian Ocean), which modulates the Indian Ocean trade winds and their control on the East African rainfall (Manatsa *et al.*, 2014). The other relevant high-pressure system whose strength, position and orientation affect weather in East Africa is the St. Helena High, located in the South Atlantic. It is responsible for the transfer of the unstable Congo air mass that contributes to rain development in East Africa (Finney *et al.*, 2019).

On longer time scales, both the Indian Ocean Dipole Mode (IODM) and the Madden–Julian Oscillation (MJO) are known to affect rainfall in East Africa (Camberlin *et al.*, 2019). However, during the case study considered in the present work (as described below), both modes were not significantly affecting rainfall dynamics in the region of interest (western Kenya). In particular, IODM was neutral (bom.gov.au/climate/enso/indices.shtml?bookmark=iod, accessed July 2020) and the Real-time Multivariate MJO

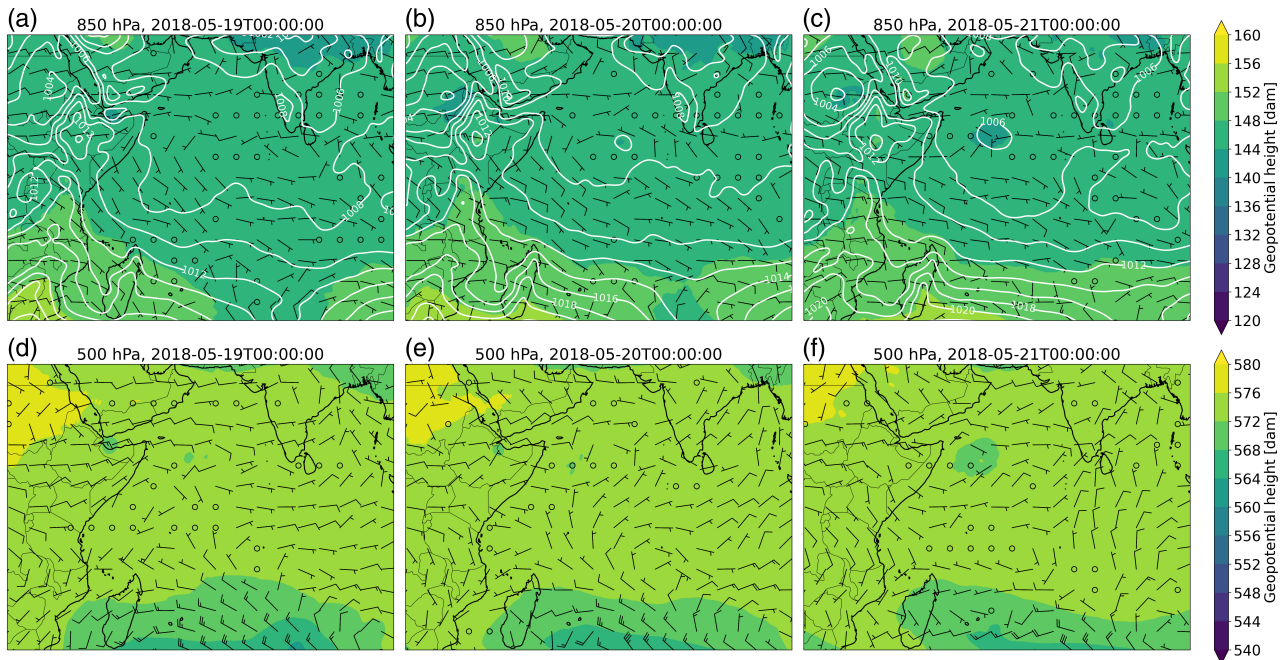


FIGURE 2 Synoptic conditions from ERA5 at 850 hPa (a)–(c) and at 500 hPa (d)–(f) over the western Indian Ocean and East Africa. In colour shading the geopotential height [dam], in white contours the sea-level pressure [hPa] and the quiver indicates the wind field ($\text{m}\cdot\text{s}^{-1}$). Black lines outline land masses and national boundaries [Colour figure can be viewed at wileyonlinelibrary.com]

(RMM) index (Wheeler and Hendon, 2004) was in a weak phase 5 (bom.gov.au/climate/mjo, accessed July 2020).

The event under study took place in the eastern part of Uganda between May 21 and 22, 2018. The Copernicus website floodlist.com reports that it caused the River Manafura to flood part of the Butaleja District, near the border with Kenya. According to local media, people were forced to evacuate their houses, crops were damaged, roads were blocked and drinking water was contaminated (<http://floodlist.com/africa/uganda-floods-eastern-region-may-2018>, accessed June 2020). Since this event struck at the end of the rainy season, the fact that the soil was very moist and unstable triggered a large hydrological response.

Figure 2 shows the synoptic situation over the western Indian Ocean and East Africa between the May 19 and 21, 2018, from ERA5 (Hersbach *et al.*, 2020). In the first row, the variables at 850 hPa indicate that over Kenya the surface wind field changes from south-easterly to easterly. This is consistent with the climatological behaviour of the region, characterised by: (a) south-easterlies that, interacting with the terrain orographic structures, form the Turkana Jet, and (b) a local circulation that features a convergence area over the Kenya–Uganda border that promotes uplift and, possibly, rainfall (Nicholson, 2016). This wind veering appears to be linked to an eastward displacement of the Mascarene High, as visible in the sea-level pressure field in the southern-most part of the panels. In the second row, the mid-tropospheric variables at 500 hPa

also show that on these days there is a significant wind veering from north-east to south-east.

The phase of heavy rainfall is observed between 1800 UTC on May 21, 2018 and 0000 UTC on May 22, 2018 (see Figure 8 for the CMORPH map of accumulated rainfall). In particular, although neither KMD nor TAHMO rain gauges captured the rainfall peak over Mount Elgon (roughly 35°E , 1°N), which is likely to be responsible for the floods in Uganda, various rain gauges along the Kenya–Uganda border recorded daily amounts of rainfall larger than 50 mm (not shown). KMD daily meteograms also recorded cumulonimbus clouds and thunderstorms with showers in the afternoon of May 21 over the highlands west of the Rift Valley. The inter-distance between TAHMO and KMD rain gauges being roughly 150–200 km, their observations are too far apart to obtain a reliable rainfall field with some form of spatial interpolation. This is why satellite rainfall estimate maps are used to validate the simulations. In particular, it seems that the satellite estimates are overestimating the ground-based observed rainfall, but they are not qualitatively in contrast with each other in the time window of the event, namely 6 hrs (not shown).

3.2 | South Africa

South Africa is located between 22° and 35°S , in the subtropics, and it is therefore influenced by weather systems

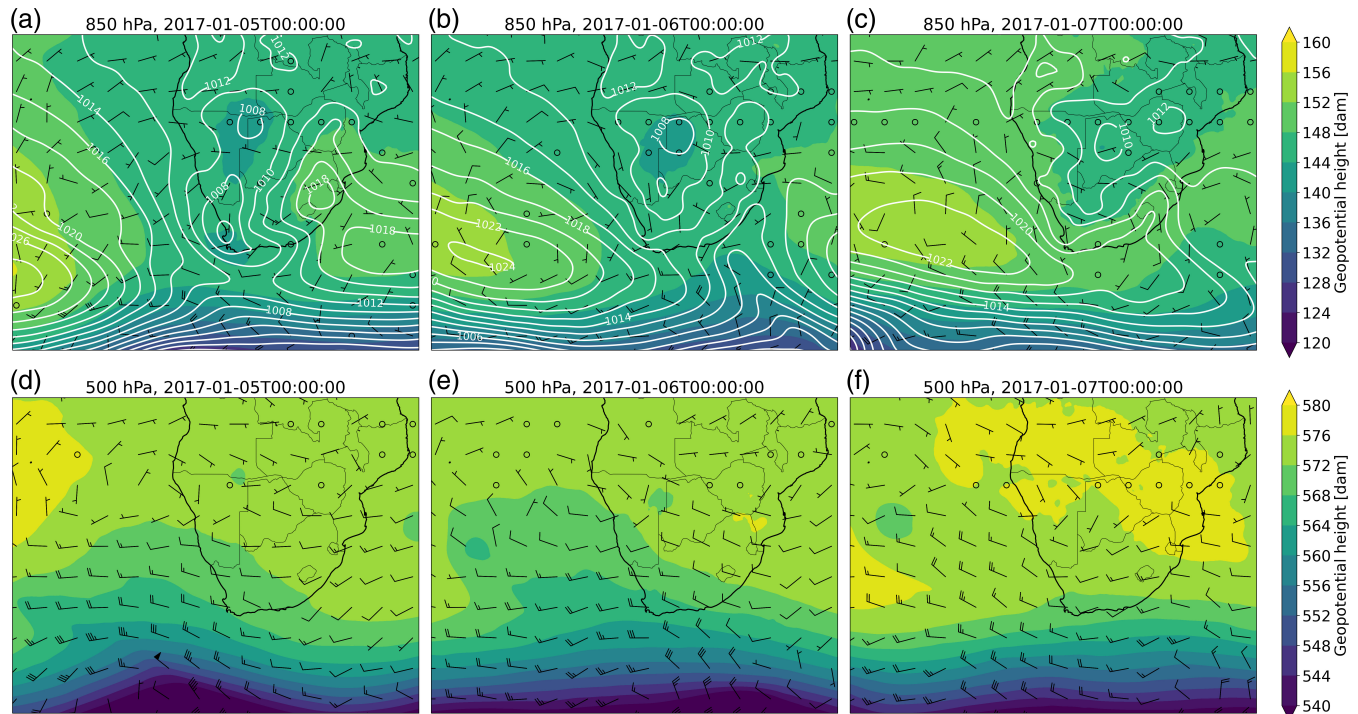


FIGURE 3 Synoptic conditions from ERA5 at 850 hPa (a)–(c) and at 500 hPa (d)–(f) over the south-eastern Atlantic Ocean and South Africa, for the January 2017 case. In colour shading the geopotential height (dam), in white contours the sea-level pressure [hPa] and the quiver indicates the wind field ($\text{m}\cdot\text{s}^{-1}$). Black lines outline land masses and national boundaries [Colour figure can be viewed at wileyonlinelibrary.com]

originating in the tropics, sub-tropics and mid-latitudes. A large part of South Africa falls within the summer rainfall region (from December to March), while the south-western parts of the country receive rainfall in winter when mid-latitude systems migrate northward (Rapolaki *et al.*, 2019). Upper air systems, in particular cut-off lows and troughs, can result in HIWEs because they promote uplift to the east of their trough axis (Ndarana *et al.*, 2020b). Very cold conditions are usually experienced across the country when these upper air systems are coupled with a surface low-pressure system associated with a cold front. When coupled with a ridging high-pressure system, heavy rainfall events are usually experienced along the eastern coastal provinces of South Africa (Ndarana *et al.*, 2020b). These systems can also result in mesoscale convective systems (MCSs) (Blamey and Reason, 2009), or larger structures, such as synoptic-scale cloud bands, also known as tropical temperate troughs (Hart *et al.*, 2010, TTTs). Tropical cyclones can also impact the region significantly when they make landfall (Malherbe *et al.*, 2012).

Numerical studies have been conducted over South Africa with a focus on heavy rainfall events. For example, Singleton and Reason (2006) study the role of the orography and the Agulhas SST in the heavy rainfall event of August 15–16, 2002, which was associated with a cut-off low system. The complex interactions between the

orography, the SST structures, the mid-level low-pressure system and the low-level moist jet all contributed to the generation of a persistent localised heavy rainfall band which caused significant damage. Singleton and Reason (2007) study a similar event, which occurred between March 23 and 24, 2003, characterised by a low-pressure system that was fuelled by the intense latent fluxes over the warm Agulhas Current. They highlight that also in this case the interactions with the orography helped to maintain the system in the same position, resulting in a high amount of rainfall. These kind of cut-off low systems are typical of the south-western coastal regions and mostly occur during the austral autumn and spring seasons (Ndarana *et al.*, 2020b). Concerning MCSs, Blamey and Reason (2009) find that a persistent low-level moisture flux, together with conditional instability and the uplift provided by surface convergence and the orography, are responsible for the development of the MCS and its intense rainfall.

Two large-scale events are considered in South Africa in the present work: the former, between January 6 and 8, 2017, which is named SA_Jan2017, is an example of a HIWE controlled by a ridging high (Ndarana *et al.*, 2018; Ndarana *et al.*, 2020a), and the latter, between March 22 and 24, 2018, which is named SA_Mar2018, is an example of a HIWE due to a cut-off low associated

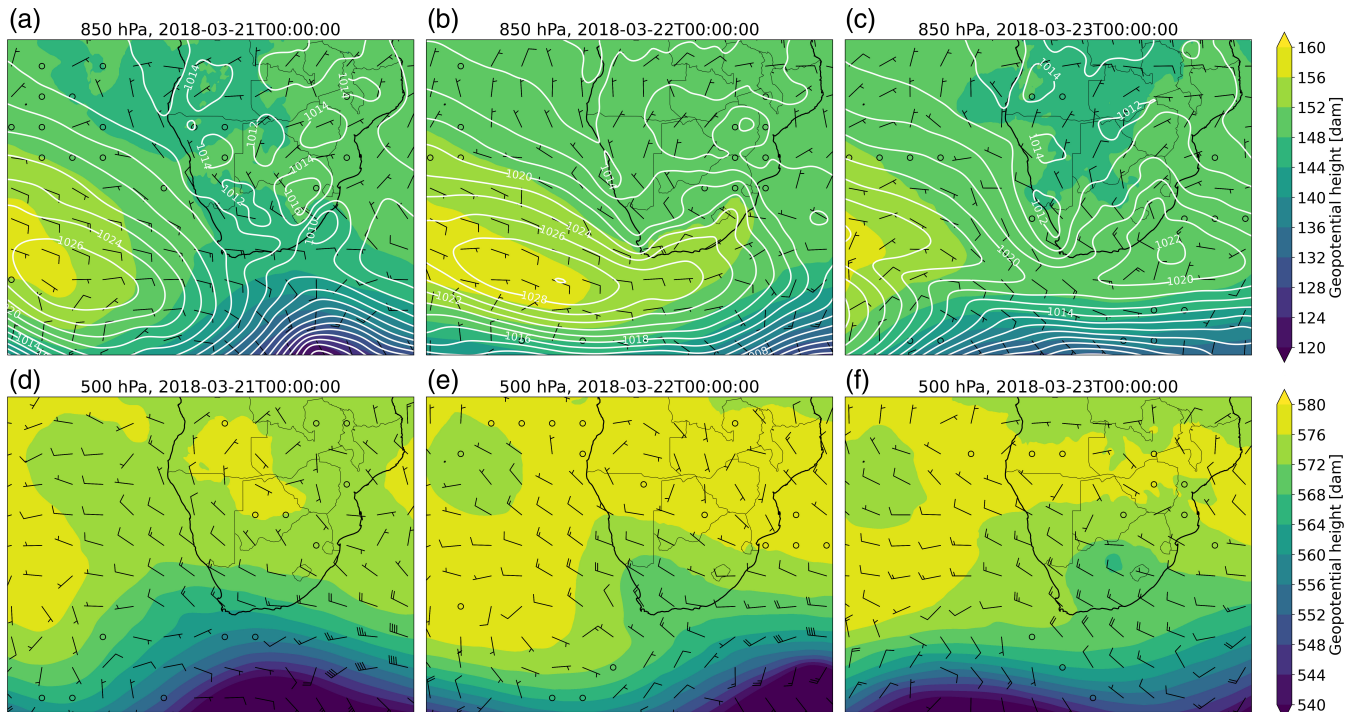


FIGURE 4 Synoptic conditions from ERA5 at 850 hPa (a)–(c) and at 500 hPa (d)–(f) over the south-eastern Atlantic Ocean and South Africa, for the March 2018 case. In colour shading the geopotential height (dam), in white contours the sea-level pressure (hPa) and the quiver indicates the wind field ($\text{m}\cdot\text{s}^{-1}$). Black lines outline land masses and national boundaries [Colour figure can be viewed at wileyonlinelibrary.com]

with a ridging high (Favre *et al.*, 2013; Ndarana *et al.*, 2020b). They both hit the north-eastern part of the country (Limpopo, Mpumalanga and Gauteng provinces) and caused extensive flooding, provoking major damage and some casualties, as reported by the news (<http://floodlist.com/africa/south-africa-floods-limpopo-mpumalanga-january-2017> for the January 2017 case; <http://floodlist.com/africa/south-africa-gauteng-floods-march-2018> for the March 2018 case, both accessed in June 2020). According to Ndarana *et al.* (2020a), ridging systems are quite typical over South Africa, and these systems contribute 60% to summer rainfall days. When they are associated with an upper air system which promotes uplift, they can produce heavy rainfall that sometimes results in flooding. Cut-off low systems are year-round events with a maximum in April and lower maxima in August and October (Ndarana *et al.*, 2020b). They promote uplift, and can increase the impact associated with surface systems including cold fronts and ridging highs.

Figures 3 and 4 show the synoptic conditions for the two events from ERA5 (Hersbach *et al.*, 2020), in agreement with the SAWS synoptic charts (not shown). The former figure displays the fields of geopotential height, wind speed at 850 and 500 hPa and surface pressure on January 5, 6 and 7, 2017. It shows a surface high-pressure system in the north-eastern part of South Africa on January 5, which

has been shown to be a climatological feature influenced by ridging highs (Ndarana *et al.*, 2020a). Low-pressure systems are present in the interior of South Africa and over the Mozambique Channel, which result in easterlies and north-easterlies over Limpopo Province. On January 6, the low over Mozambique moves inland over Zimbabwe and Zambia. By January 7, the Atlantic Ocean high ridges on the eastern parts of the country, producing low-level moisture transport from the relatively warm Agulhas Current waters inland. An eastward approaching trough is visible in the mid–upper troposphere (at 500 hPa), associated with wind divergence at the same height. This dynamics is different from what is observed for the March 2018 case (Figure 4), where the mid-tropospheric trough is more pronounced (especially on March 22) and is associated with an easterly surface flow off the coasts of South Africa, and a north-easterly flow over land. This is driven by an anticyclonic cell in the Mozambique Channel that brings warm and moist air from the tropical Indian Ocean, generating areas of strong surface convergence in the interior of the country. The ridging Atlantic high is visible in the surface pressure field on March 22, while the cut-off low appears on March 23 in the 500 hPa field.

A rainfall structure elongated along the NW–SE direction is produced in both cases. Forty-hour accumulated rainfall fields are shown in the following section, between

2018-05-21 12:00:00

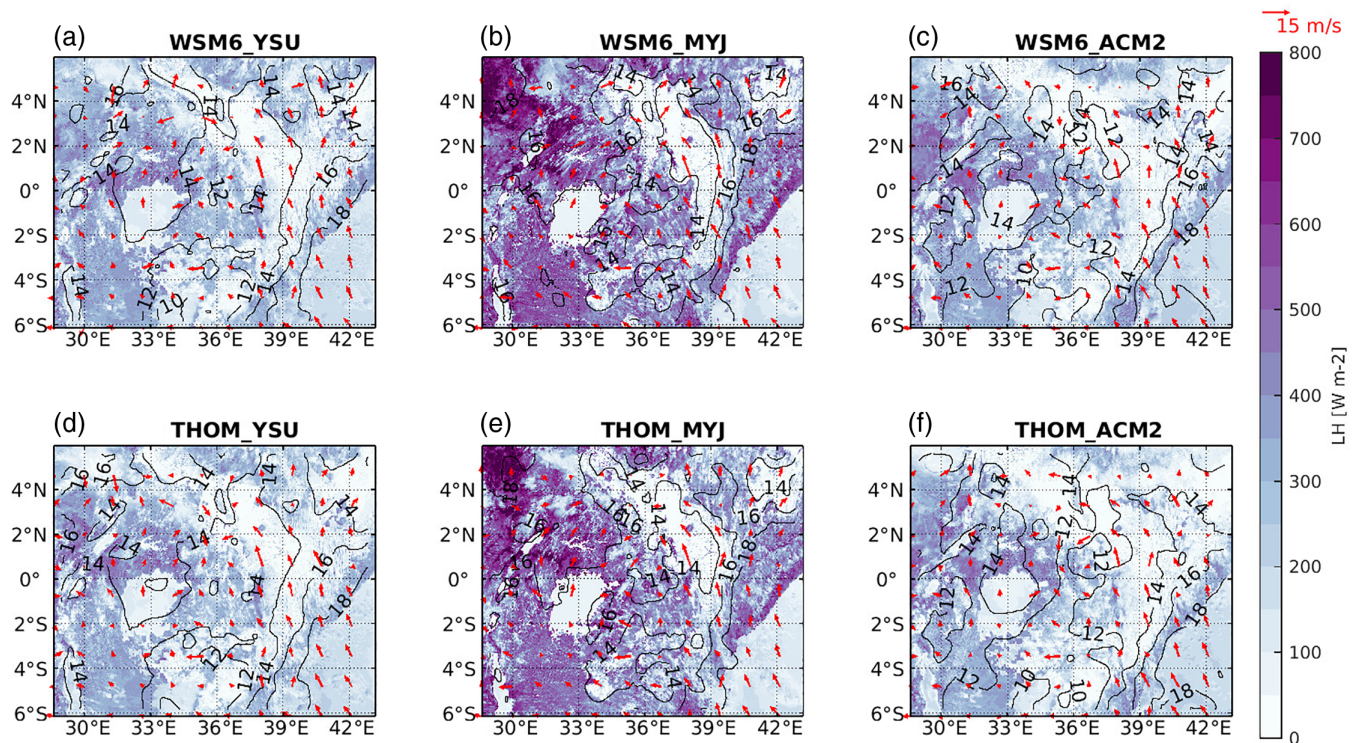


FIGURE 5 Surface latent heat flux (LH [$\text{W}\cdot\text{m}^{-2}$], colour shading), 10-m wind field (vectors) and smoothed 2-m water vapour mixing ratio ($\text{g}\cdot\text{kg}^{-1}$) from the six configurations under study at 1200 UTC on May 21, 2018. A reference arrow for the surface wind field is shown in the upper-right corner [Colour figure can be viewed at wileyonlinelibrary.com]

0000 UTC on January 6 and 0000 UTC on January 8, 2017, and between 0000 UTC on March 22 and 0000 UTC on March 24, 2018, for the two HIWEs under study.

4 | VALIDATION AND RESULTS

The skills of the various configurations are firstly analysed by comparing some simulated instantaneous maps of the following variables: 10-m wind field, surface latent heat flux, hourly rainfall, convective available potential energy (CAPE) and 2-m water vapour mixing ratio (Q2). Satellite daily mean CTT values are used to assess how the different configurations reproduce the observed cloud field properties. For the South African case studies, a comparison of the vertical profiles of potential temperature and water vapour mixing ratio with respect to some of the available radiosonde observations is then performed.

The simulations are then validated in terms of accumulated rainfall with the Method for Object-Based Diagnostic Evaluation (MODE) (Davis *et al.*, 2006a; 2006b). This method identifies precipitation objects, based on a threshold on the accumulated rainfall amount, in both forecast and observation rainfall fields. Then, some geometrical

indices are calculated, so that the forecast and observed objects can be compared quantitatively. In this way, the well-known double-penalty issue that traditional verification methods suffer from is avoided (Ebert, 2008). Here the geometrical indices of interest are listed, with their best score in brackets: CENTROID_DIST (0): difference between the centres of mass of the two objects, measuring the model skills in terms of localisation of the event; ANGLE_DIFF (0): difference between the orientation (i.e., the angle that the longest side of the object forms with the model grid) of the two objects; AREA_RATIO (1): ratio of the areas of the two objects, which together with the next two indices measures the skills of the model in terms of spatial extent of the forecast; INTERSECTION_AREA (area of the observed object): area of the overlap of the two objects; UNION_AREA (area of the observed object): union (as defined in set theory) of the areas of the two objects; PERCENTILE_INTENSITY_RATIO (1): ratio of the 90th percentiles of the forecast rainfall intensity and the observed one. Note that some metrics, such as ANGLE_DIFF, can show a strong dependence on the resolution of the fields under study and can, therefore, introduce a certain degree of arbitrariness in the evaluation. Keeping this in mind, however, by considering all

2018-05-21 12:00:00

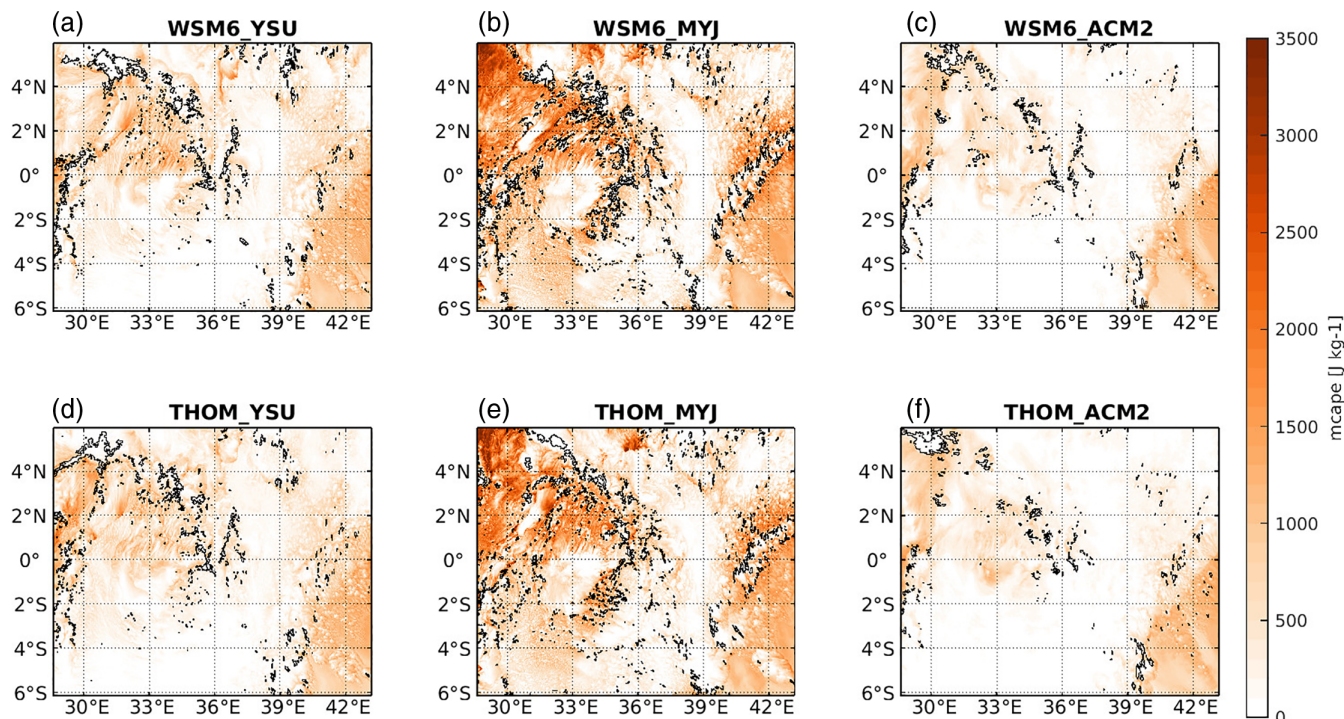


FIGURE 6 Maximum CAPE (mcape, colour shading) and hourly rainfall field (black contour line at 5 mm-hr^{-1}) from the six configurations under study at 1200 UTC on May 21, 2018 [Colour figure can be viewed at wileyonlinelibrary.com]

the calculated geometrical indices, the MODE tools can provide useful insights on the model performances.

4.1 | Kenya–Uganda

As discussed in Section 3.1, the KU_May2018 event is representative of the rainfall climatology of the MAM rainfall season in East Africa (Nicholson, 2016). In fact, the south-easterly winds that bring moisture inland from the Indian Ocean impinge on the terrain features and create a zone of surface convergence over the relief along the Kenya–Uganda border. The low-level wind structure is visible in Figure 5, which displays the modelled 10-m wind field at 1200 UTC on May 21, 2018 (a few hours before the beginning of the rainfall event) obtained from the six configurations under study. The colour shadings in Figure 5 show the surface latent heat flux, which appears significantly more intense in the two configurations with the MYJ PBL scheme (Figure 5b, e). The larger latent heat flux of the MYJ simulations corresponds to higher values of low-level moisture (shown as 2-m water vapour mixing ratio, Q2, with the black contour lines in Figure 5). In terms of Q2, WSM6_ACM2 appears as the driest configuration among those considered in this study. Figure 6, then,

indicates that in the MJY simulations the atmosphere is more unstable than in the other configurations, with higher values of maximum CAPE (mcape) in the area surrounding Lake Victoria (especially to the north-west), over the Kenya–Uganda border and along the Indian Ocean coastlines. The increased low-level moisture of the MYJ configurations is also accompanied by a slightly reduced convective inhibition (CIN), especially over land, that is thought to be responsible for a premature triggering of convection. A lot of rainfall (black contour lines in the same figure) is simulated in the MYJ configurations in the areas of high atmospheric instability, suggesting that the stronger daytime latent heat flux in the MYJ scheme generates too much instability, which is responsible for spurious rainfall in the hours preceding the actual rainfall event.

The fact that the atmosphere simulated with the MYJ scheme is more prone to vertical motion can be also inferred by looking at the daily CTT values in Figure 7. In fact, colder daily values of CTT are simulated in the MYJ configurations with respect to the others. Although the simulations are not able to properly represent the observed clouds, it generally appears that WSM6 produces colder clouds than THOM. Note that cold clouds can be either produced by deep convective clouds or by thin non-precipitative cirrus clouds, thus no attempt is made

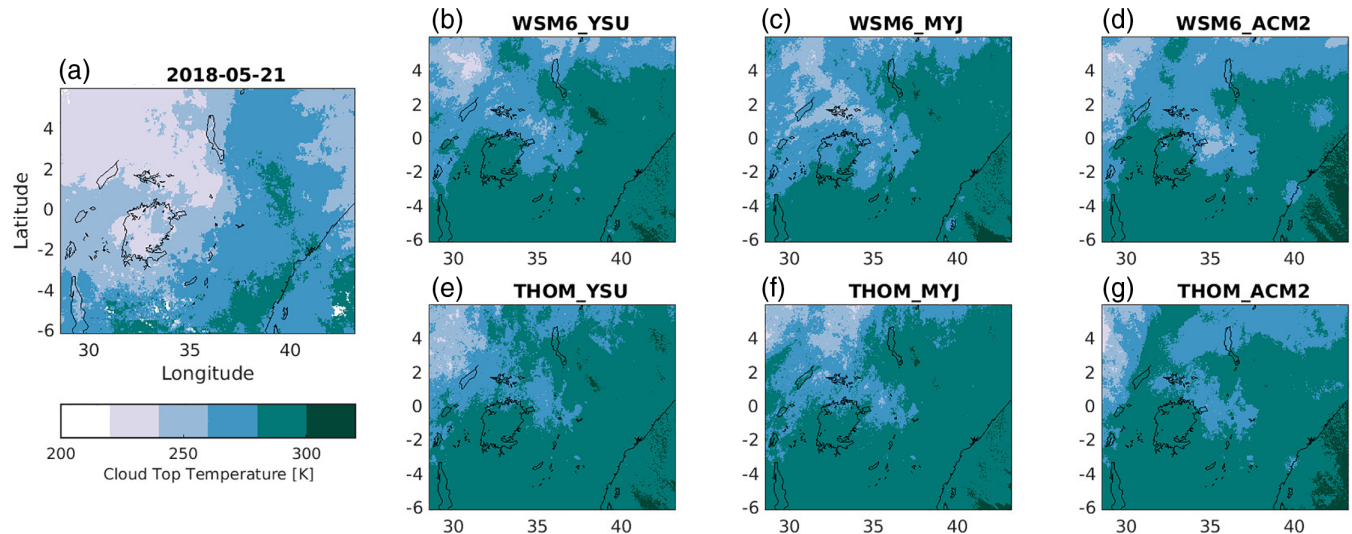


FIGURE 7 Daily average CTT on May 21, 2018: (a) measured by SEVIRI and (b–g) simulated [Colour figure can be viewed at wileyonlinelibrary.com]

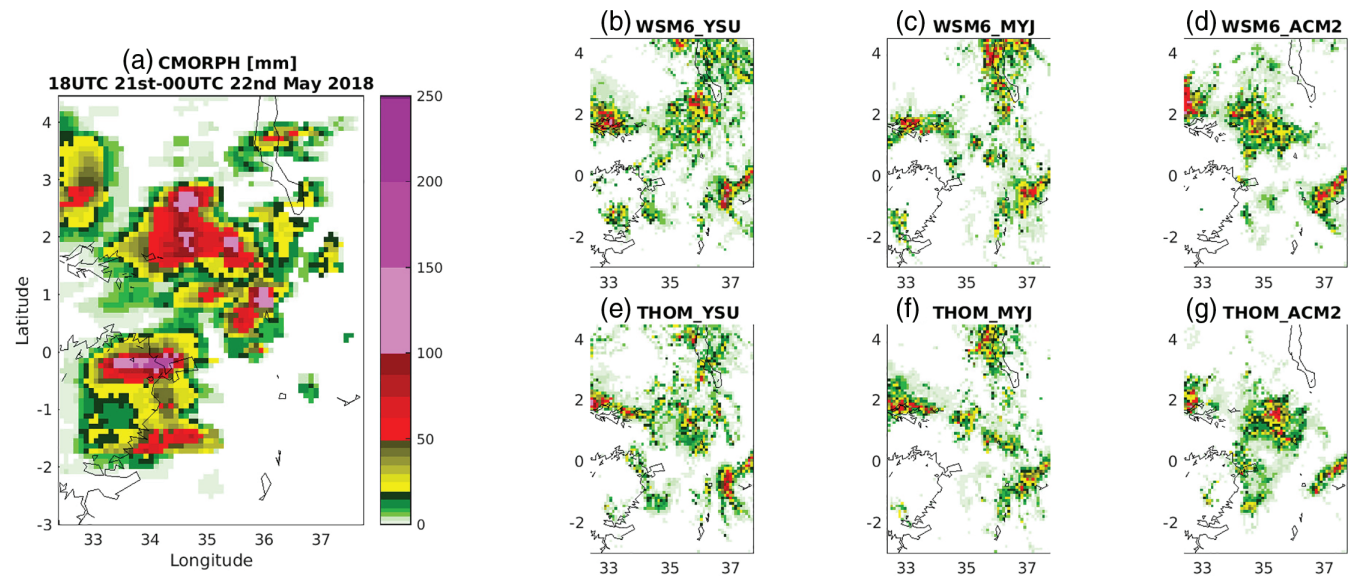


FIGURE 8 Accumulated rainfall depth in the time frame and region of interest for the KU_May2018 case. (a) CMORPH observations, (b)–(f) model simulations, as indicated in their title

here to link the CTT field with the rainfall properties. The comparison is done between the simulated and observed CTT fields to try to assess the skills of the models in reproducing the cloud distribution and properties on a daily scale.

The time frame in which the heavy rainfall event took place is between 1800 UTC on May 21 and 0000 UTC on May 22, 2018. Figure 8 shows the CMORPH observed accumulated rainfall, and the corresponding simulated fields. It is evident that all the model runs underestimate the precipitation, and miss the rainfall peak over Lake Victoria. However, the two set-ups with ACM2 PBL produce

a rainfall area over Mount Elgon (on the Kenya–Uganda border) that realistically represents the rainfall area under study. The low rainfall amount in the study area simulated by the MYJ configurations is ascribed to the fact that they both simulate spurious rainfall in the hours preceding the event, because of a too unstable atmospheric column, as discussed above.

For a quantitative assessment of the model performances, the outlines of the forecast and modelled objects identified by MODE on the 18-mm accumulated rainfall threshold are shown in Figure 9a–f, together with their geometrical indices shown in Figure 9g–l. Note that the

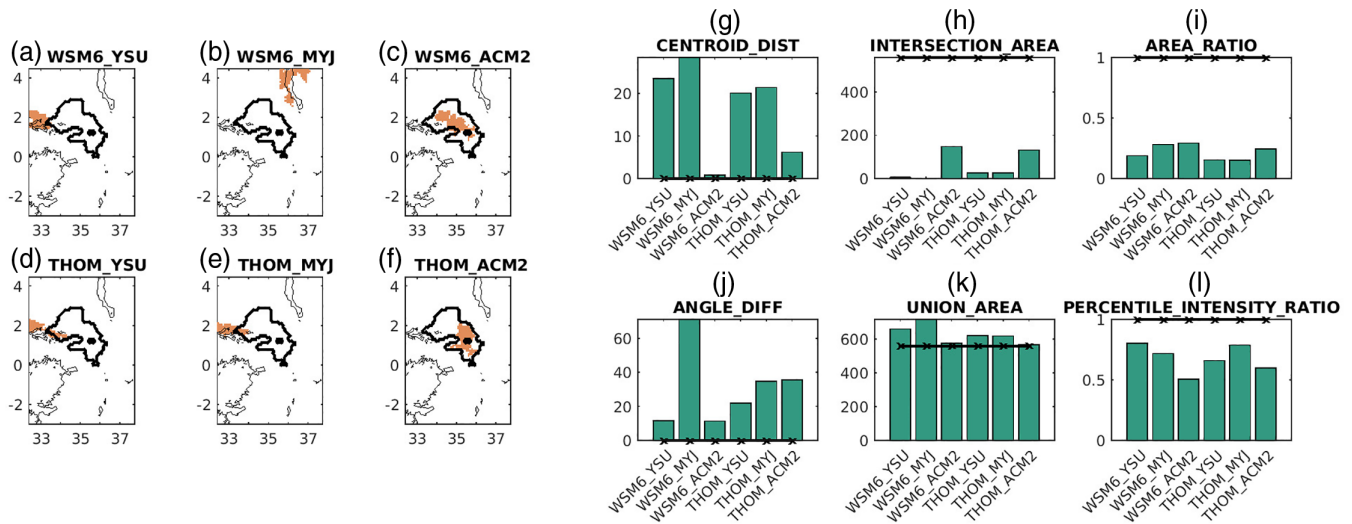


FIGURE 9 (a)–(f): Outlines of the observed object in the CMORPH field for the KU_May2018 case study (black lines), together with the simulated objects (orange shaded areas) for the different model configurations. (g)–(l) Corresponding MODE indices (best score indicated with the black lines with the crosses) [Colour figure can be viewed at wileyonlinelibrary.com]

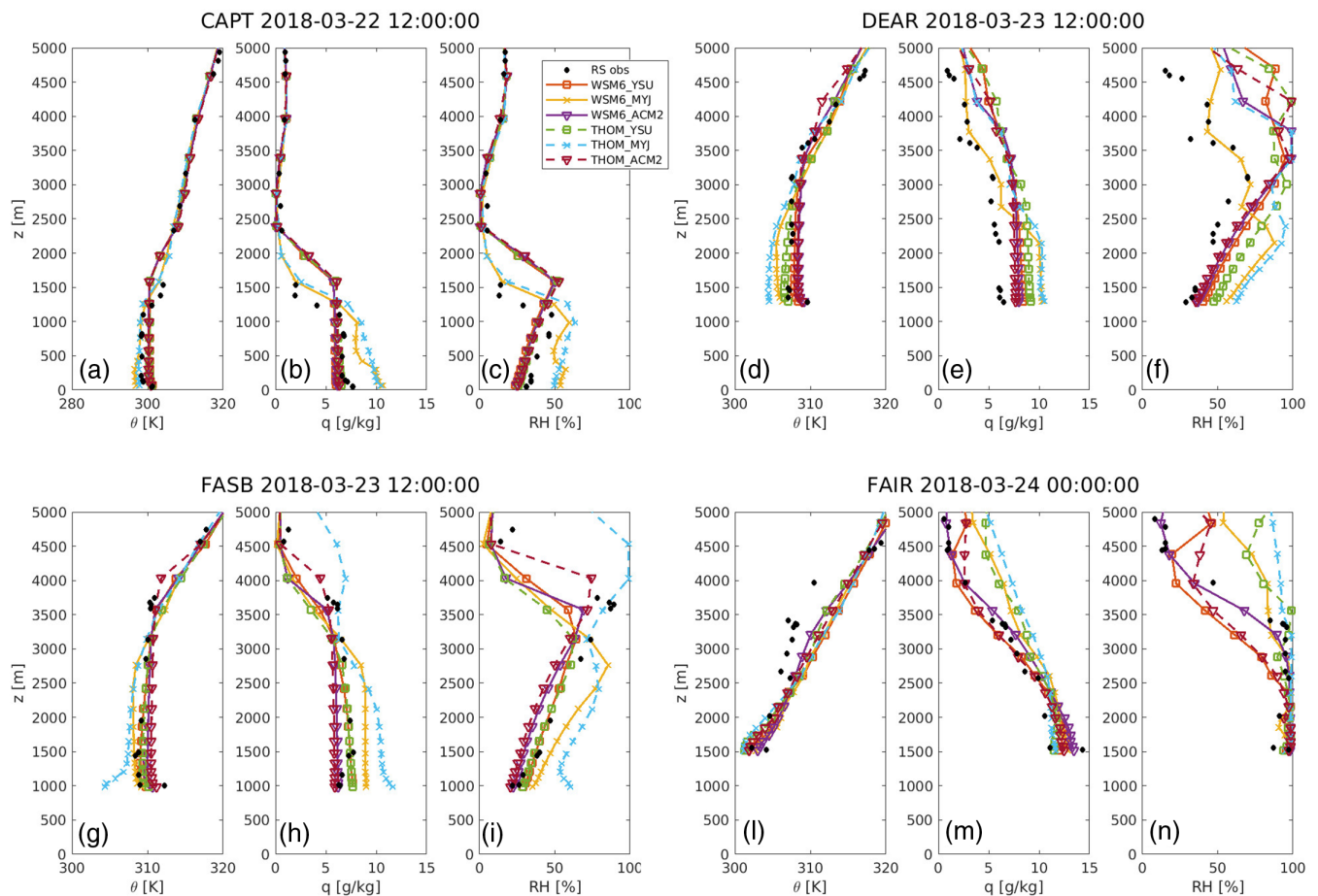


FIGURE 10 Radiosonde profiles from four different stations during the March 2018 South African case study. The location and time of the observations are indicated in the titles using the station codes shown in Figure 1a. The vertical profiles of the following variables are shown: (a), (d), (g), (l) potential temperature, θ [K]; (b), (e), (h), (m) water vapour mixing ratio, q [$\text{g}\cdot\text{kg}^{-1}$]; (c), (f), (i), (n) relative humidity, RH [%] [Colour figure can be viewed at wileyonlinelibrary.com]

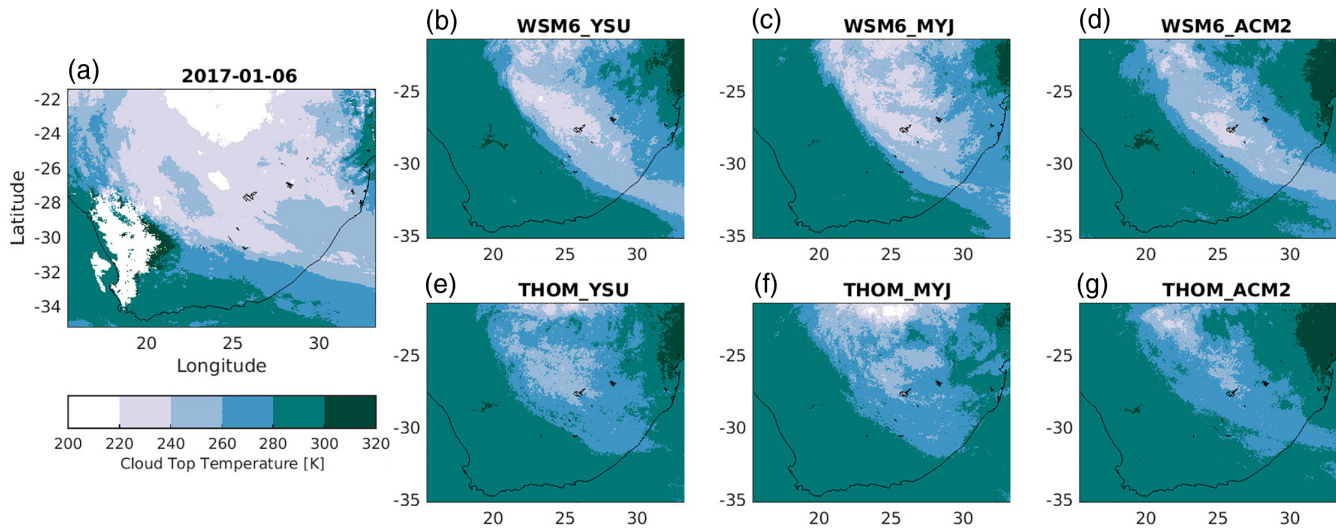


FIGURE 11 Daily average CTT on January 6, 2017: (a) measured by SEVIRI and (b–g) simulated [Colour figure can be viewed at wileyonlinelibrary.com]

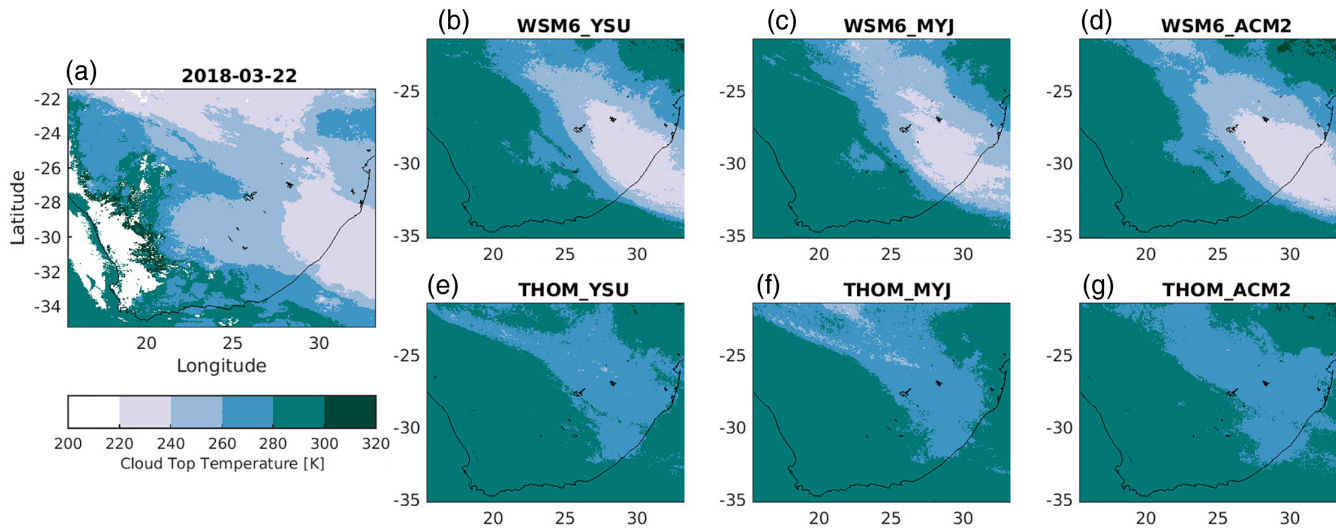


FIGURE 12 Same as the previous figure, with data shown for March 22, 2018 [Colour figure can be viewed at wileyonlinelibrary.com]

indices are calculated on the largest object identified in the region of interest, which is selected based on the observed rainfall field and is smaller than the WRF d03 numerical domain. The rationale behind this choice is that the goal is to evaluate the model skills in terms of the core rainfall simulated object.

MODE analyses identify the WSM6_ACM2 experiment as the best one. In fact, the very good overlap between the observed and the forecast objects shown in Figure 9c is confirmed by the very good indices shown in panels Figure 9g–l. In terms of location of the rainfall area, WSM6_ACM2 outperforms the other experiments (Figure 9g). It simulates a rainfall object that covers the corresponding observed one best (Figure 9h, i, k), and differs in orientation with respect to the observed rainfall

area by an angle smaller than 20° (Figure 9j), having the best performance also with respect to this metric. Figure 9cl shows that, in the WSM6_ACM2 run, the peak rainfall intensity is underestimated by a factor of 2, which is indeed a weakness of the forecast. However, from an early-warning system standpoint, it is very likely that, with an appropriate hydrological model, since the location and extent of the rainfall area is correctly captured by the simulation, this would lead to the issuance of a hydrological alert. As this goes beyond the scope of the present work, it will be the object of future analysis.

It is interesting to note that the second best configuration, with very good skills in terms of localisation and spatial extent of the forecast (Figure 9g, h, i, k) is THOM_ACM2, that is, the other configuration with ACM2

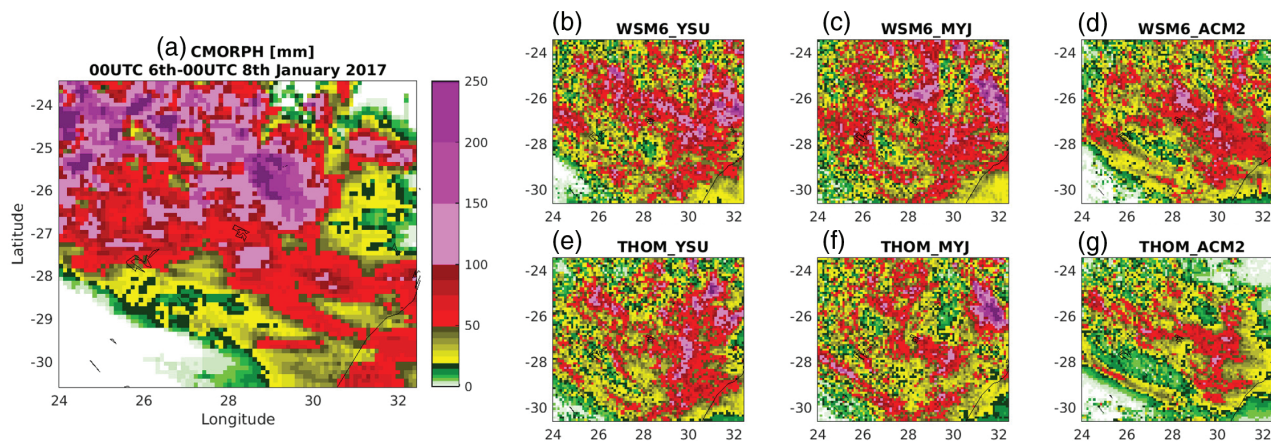


FIGURE 13 Accumulated rainfall depth in the time frame and region of interest for the SA_Jan2017 case. In the left-most panel the data are from CMORPH observations, and in the other panels, they come from the six model configurations studied (as indicated in their title)

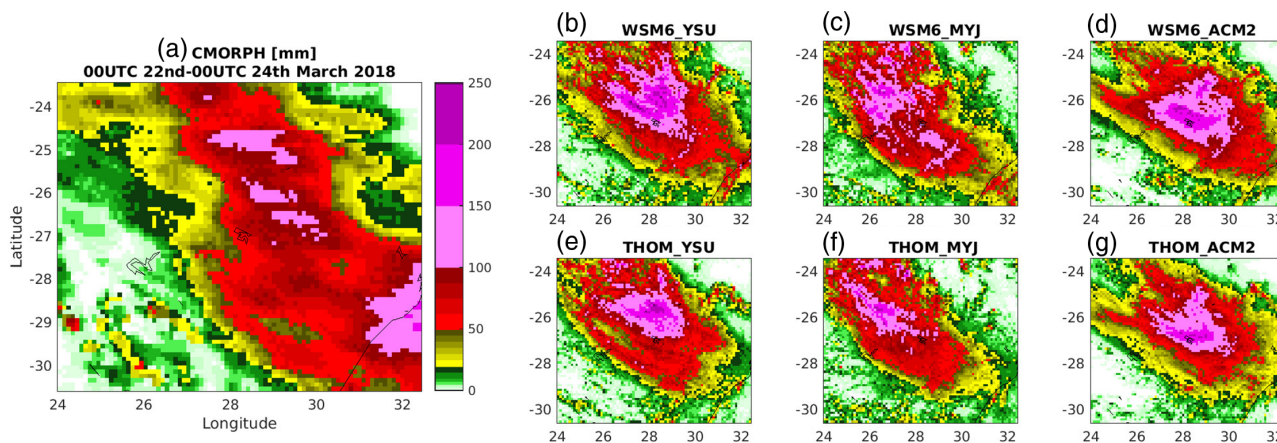


FIGURE 14 Accumulated rainfall depth in the time frame and region of interest for the SA_Mar2018 case. In the left-most panel the data are from CMORPH observations, and in the other panels, they come from the six model configurations studied (as indicated in their title) [Colour figure can be viewed at wileyonlinelibrary.com]

PBL. On the other hand, both experiments with the MYJ PBL scheme appear to have the poorest performances, as visible from the accumulated rainfall fields of Figure 8 and confirmed by the scores shown in Figure 9. These results indicate that, in this case study, the PBL scheme seems to be more important in controlling the rainfall simulation, with respect to the choice of the MP. In particular, the non-local ACM2 PBL scheme has better performances than the local MYJ one. Very similar results can be obtained by validating with respect to the IMERG Final product (not shown).

4.2 | South Africa

The South African case studies enable deeper understanding of the vertical atmospheric structure simulated by

the different numerical schemes, as radiosonde measurements are available. In the first place, by cross-comparing the instantaneous maps of latent heat, low-level moisture, wind field, maximum CAPE and hourly rainfall (not shown), similar conclusions to the KU_May2018 ones can be drawn. In particular, it is found that the configurations with the MYJ scheme produce higher low-level moisture, which is associated with stronger conditional instability and spurious rainfall.

Figure 10 shows vertical profiles of potential temperature, water vapour mixing ratio and relative humidity, comparing the modelled data with some of the available observations for the SA_Mar2018 case study. Model data are obtained by taking the vertical grid column nearest to the radiosonde station. In general, despite being derived from instantaneous fields at a single location, the agreement between the model data and the radiosonde

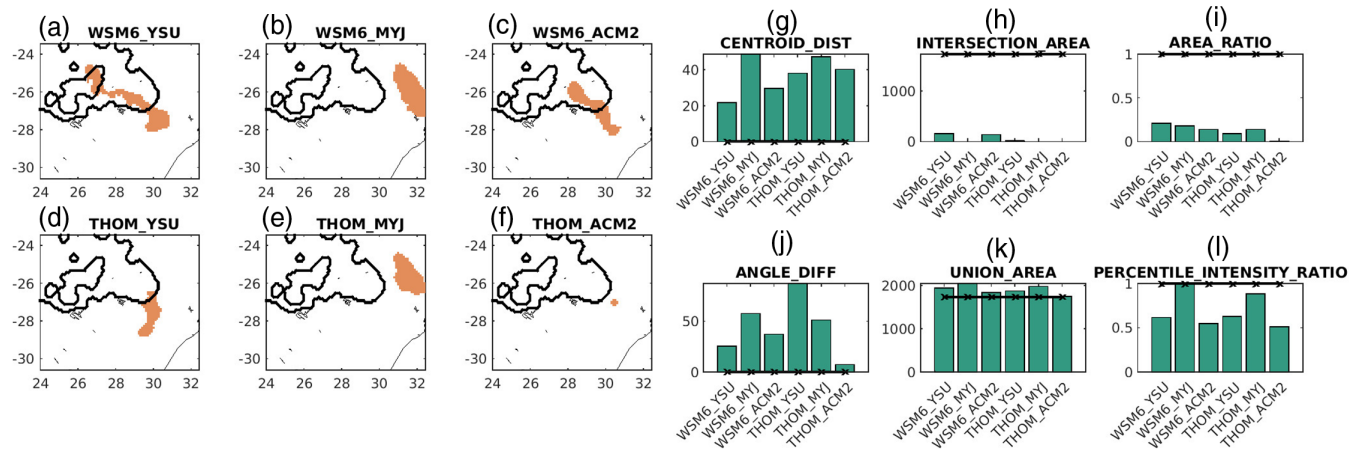


FIGURE 15 (a)–(f) Outlines of the observed object in the CMORPH field for the SA_Jan2017 case study (black lines), together with the simulated objects (orange shaded areas) for the different model configurations. (g)–(l) Corresponding MODE indices (best score indicated with the black lines with the crosses) [Colour figure can be viewed at wileyonlinelibrary.com]

observations is good. The profiles shown here are selected because they describe the common behaviour of the different WRF configurations observed during the South African case studies. In particular, on the one hand, the two non-local PBL schemes (YSU and ACM2) generally produce realistic low-level moisture values (as in Figure 10b, h, m), but a too high PBL (e.g., Figure 10b). On the other hand, the local MYJ scheme does a better job in describing the top of the PBL (as in Figure 10b, e), but often shows an overestimation of the water vapour mixing ratio in the lower layers (Figure 10b, e, h). This is interpreted to result from higher surface latent heat forcing and lower vertical mixing (due to the absence of the effect of large eddies) in the MYJ configurations. In terms of potential temperature, MYJ is found to produce cooler values (Figure 10a, d, g), that, combined with the low-level higher water vapour mixing ratio, result in significantly higher relative humidity (Figure 10c, f, i). Sometimes, the higher moisture content produced by the MYJ scheme is also visible at higher altitudes (Figure 10h, m), with corresponding high relative humidity in the mid troposphere, as well, as in Figure 10n.

The higher atmospheric moisture and corresponding higher relative humidity in the MYJ configurations is confirmed by the daily CTT comparison between SEVIRI data and the different configurations shown in Figures 11 and 12. In fact, for the same MP scheme, the configuration with MYJ has the coolest CTT values (Figures 11c, f and 12c, f). Moreover, a different structure appears in the CTT field of the two case studies. In particular, in March 2018, the CTT structure is more organised, forming a relatively smoother field, while in January 2017, it appears noisier, suggesting that more convective activity took place. Then, in the SA_Jan2017 case, CTT values are generally cooler and the

area of CTT below -40°C is larger compared with the SA_Mar2018 case, indicating, once again, that the former case is characterised by more convection. These figures also highlight that the WSM6 MP (Figures 11b–d and 12b–d) is more accurate in reproducing the observed CTT field compared with the THOM scheme (Figures 11e–g and 12e–g). By looking, for example, at the March 2018 case (Figure 12), it is clear that the elongated and relatively deep cloud structure is well represented by the WSM6 simulations, while it is significantly underestimated by the configurations with the THOM MP.

The accumulated observed and simulated rainfall fields are shown in Figures 13 and 14 between 0000 UTC on January 6 and 0000 UTC on January 8, 2017, and between 0000 UTC on March 22 and 0000 UTC on March 24, 2018, respectively.

In terms of accumulated rainfall validation, in both cases the time period is 48 hrs and the threshold is set to 80 mm. As the events are driven by the large scale, a convolution radius of three grid steps is used in the MODE object identification procedure to correctly capture the largest core object in the rainfall field. Figures 15 and 16 show the objects identified by MODE for the observed and simulated rainfall fields, together with their corresponding geometrical indices.

For the January 2017 case study (Figure 15), all configurations simulate the intense rainfall object over a significantly smaller area compared with the observations. Among the experiments, the WSM6_YSU and WSM6_ACM2 configurations appear to model the core precipitating area best (Figure 15a, c). In fact, they are characterised by the best CENTROID_DIST index (Figure 15g), indicating good location of the rainfall object, as well as good INTERSECTION_AREA (Figure 15h)

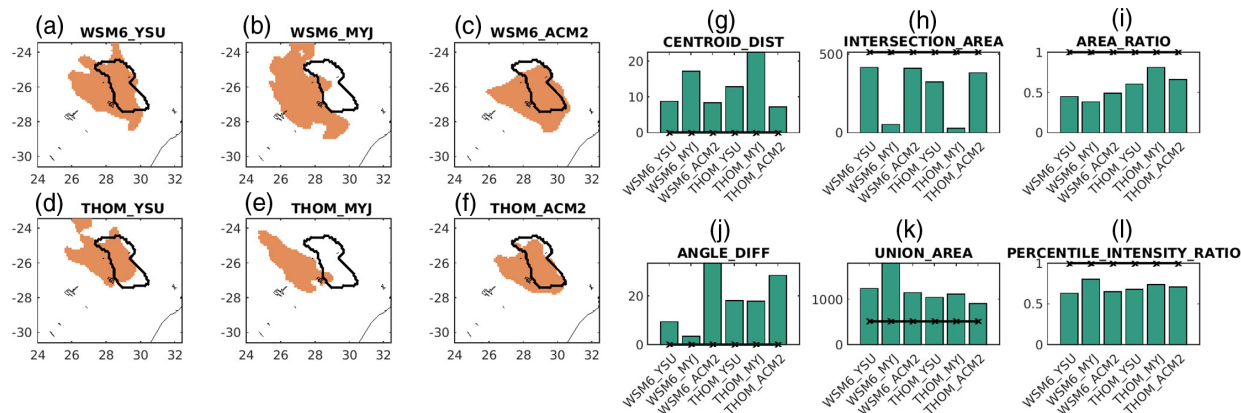


FIGURE 16 (a)–(f): Outlines of the observed object in the CMORPH field for the SA_Mar2018 case study (black lines), together with the simulated objects (orange shaded areas) for the different model configurations. (g)–(l) Corresponding MODE indices (best score indicated with the black lines with the crosses) [Colour figure can be viewed at wileyonlinelibrary.com]

and UNION_AREA (Figure 15k) indices, suggesting a relatively good spatial extent of the intense rain forecast. Also in terms of the orientation of the forecast object, WSM6_YSU and WSM6_ACM2 have the best scores (Figure 15j, note that THOM_ACM2 has a better ANGLE_DIFF score, but it is not relevant because it corresponds to a very small object, see Figure 15f). These two configurations share the same MP scheme and the fact that the PBL scheme is non-local. As for the KU_May2018 case study, the MYJ experiments appear to have the poorest performances, with a misplaced forecast rainfall object (Figure 15g, h, k) which underestimates the observations (Figure 15l). This behaviour is interpreted to be caused by the larger conditional instability simulated by this PBL scheme, which makes the atmosphere more prone to produce rainfall, resulting in a spatio-temporal mismatch with respect to the observations. The PERCENTILE_INTENSITY_RATIO scores (Figure 15l) indicate that the MYJ PBL scheme better reproduces the peak rainfall values, irrespective of the MP choice.

From the MODE analyses for the SA_Mar2018 case study, shown in Figure 16, it emerges once again that the MYJ scheme has the lowest performances, since the overlap between the rainfall objects is clearly worse for this PBL scheme than for the other two choices (Figure 16a–f). Also in this case study, the simulations all underestimate the observed rainfall depth (Figure 16l). The location and extent of the core rainfall area are very well captured by the ACM2 configurations, with THOM MP being generally better than WSM6 (Figure 16g, i, k). Also WSM6_YSU is characterised by good geometrical scores, especially in terms of orientation of the rainfall object (Figure 16j). As for the KU_May2018 case study, similar results can be obtained by validating the simulations with respect to the IMERG Final rainfall product (not shown).

5 | CONCLUSIONS

A set of six experiments with two MP schemes and three PBL schemes is performed for three representative case studies of heavy rainfall in Sub-Saharan Africa with a cloud-resolving NWP model, WRF. The events are selected because they recently hit some of the target countries of the TWIGA project, causing widespread damage and seriously affecting society. High-resolution numerical simulations of such events can be a powerful tool to inform the issue of warnings and alerts to the population, so that injury, loss of life and damage to property can be reduced. However, in the case of heavy rainfall, simulations are very sensitive to the choice of physical parameterisations, with different schemes being optimised for different geographical settings and atmospheric dynamics. The goal of this work is to assess the forecasting performances of cloud-resolving simulations for some relevant numerical schemes in this region of the world.

Maps of surface latent heat, low-level moisture and maximum CAPE show that the only local PBL scheme, MYJ, is characterised by stronger daytime latent heat flux, which produces excessive low-level moisture (sometimes extending to the top of the PBL), which makes the air column more unstable. This generates spurious rainfall that results in large spatio-temporal bias in terms of the core rainfall simulation. Not only is MYJ the only local PBL scheme, meaning that it lacks the representation of the vertical mixing due to large eddies, but it also has a different surface layer model. In fact, a Mellor–Yamada level 2 turbulence closure is implemented in the MYJ formulation, instead of the more common similarity approach used with YSU and ACM2. Comparisons of the model data with available radiosonde observations in South Africa confirm that MYJ generally produces higher values of moisture (especially in the low levels), which combined

with a slightly negative bias in potential temperature, results in large deviation of relative humidity with respect to the observations.

A correct representation of the atmospheric humidity field is of paramount importance for heavy rainfall simulations, as water vapour spatio-temporal distribution plays a crucial role in the rainfall dynamics. Ralph *et al.* (08 2013), for example, show how important the PBL and LSM schemes are in determining the low-level moisture content, which controls the development of convection and its subsequent rainfall. Their results agree with the implications of the plots and the radiosonde comparisons discussed above, which demonstrate how an incorrect low-level moisture content leads to a misrepresentation of the rainfall structure. However, if in Ralph *et al.* (08 2013) the low-performing schemes were found to typically produce insufficient amounts of low-level moisture, here the MYJ PBL scheme is found to have poor performances because it produces excessive low-level moisture, enhancing the atmospheric instability and producing spurious rainfall. Future studies will consider the sensitivity to LSM schemes, as well.

The skills of the six selected configurations are quantitatively assessed using two of the most reliable satellite products in Sub-Saharan Africa (IMERG, not shown explicitly, and CMORPH). In particular, some geometrical indices of appropriately defined objects in the simulated rainfall field are compared with the corresponding observed ones with a state-of-the-art validation tool, namely MODE. In the case studies analysed, it is generally found that the PBL scheme has a stronger control on the rainfall structure than MP, which is in line with the findings of Flaounas *et al.* (2011) and Kouadio *et al.* (2018). This can be interpreted with the fact that the vertical mixing in the lower atmosphere has a prominent role in determining the air mass properties, which then, through the MP scheme, produce the hydrometeors that form precipitation.

In principle, both MP schemes selected in this work are suitable for convection-permitting model configurations and are both optimised to properly interact with the RRTMG RAD scheme, selected here. WSM6 is a single-moment scheme, meaning that only the mass variable equations are treated, and not the number concentration variable ones (as in the double-moment schemes). THOM MP, instead, has a double moment approach for some of the hydrometeors. However, it has been developed for mid-latitude simulations, and this might be the reason why in the African case studies selected here WSM6 appears to perform equally well or better than THOM. In particular, it is found that WSM6 simulations outperform THOM ones in terms of CTT simulation, irrespective of the PBL choice. THOM is found to systematically overestimate

the daily average CTT, indicating the simulation of shallower clouds. It may be noted that WSM6 is the scheme used in the WRF Tropical suite, while THOM is used in the CONUS (CONtinentaL United States) one. Despite the limited number of case studies considered here, the systematic behaviour in terms of CTT supports this choice.

Concerning the PBL scheme, all the experiments highlight persistent poor capabilities of MYJ in simulating the rainfall field, especially in terms of intense rainfall location. In this work, MYJ is the only local PBL scheme, meaning that it does not explicitly include the vertical transport by large eddies. The fact that it has the poorest performances, thus, is physically consistent with the importance of vertical transport (of mass, water and energy) in heavy rainfall dynamics, especially when convection takes place. YSU and ACM2, instead, are non-local schemes that treat the vertical transport by large eddies with a counter-gradient term and a mass-flux term, respectively. They show very good and similar performances, with the latter behaving visibly better in the Kenya–Uganda case study. ACM2 is suggested as a PBL scheme for event-based studies in East Africa by Sun *et al.* (2015). Also, Noble *et al.* (2014) and Noble *et al.* (2017) indicate it as the best-performing PBL scheme in their extensive sensitivity studies, also noting that MYJ has poor performances. The fact that non-local schemes are more suitable in this region of the world is also highlighted by Meynadier *et al.* (2015) and Kouadio *et al.* (2018). The local MYJ PBL scheme is not recommended also by Crétat *et al.* (2012), and its tendency to produce spurious rainfall is also acknowledged by its author (Janjic, 1994).


In conclusion, the identified best-performing setup for HIWE simulations in terms of MP choice uses the WSM6 scheme. The PBL scheme appears to have a more prominent role for a correct location of the intense rainfall, and its choice is in line with previous results in literature, even if they are mostly focused on seasonal and climatic time scales. Namely, non-local PBL schemes (YSU and ACM2) should be preferred instead of local ones (such as MYJ). With respect to the WRF tropical suite suggested in the community (Wang, 2017), it is found that, at convective-resolving scales, the ACM2 PBL scheme performs better than the YSU one. For this reason, we advocate more heavy rainfall sensitivity studies over the under-explored African continent to further test the relative ability of these two PBL schemes.


ACKNOWLEDGEMENTS

The authors declare no conflict of interest. This work was mostly funded by the TWIGA project, which has received funding from the European Union's Horizon 2020 Research and Innovation Programme under grant agreement no. 776691. Thanks are due to LRZ Supercomputing


Centre, Garching, Germany, where the numerical simulations were performed on the SuperMUC Petascale System, Project-ID: pr62ve. TAHMO and SAWS are acknowledged for providing the ground-based sensor data. The authors are grateful for the careful revision of two anonymous reviewers.

ORCID


Agostino N. Meroni  <https://orcid.org/0000-0001-5504-632X>

Mary-Jane Bopape  <https://orcid.org/0000-0003-2111-4595>

Thizwilondi R. Maisha  <https://orcid.org/0000-0002-4941-8016>

Martina Lagasio  <https://orcid.org/0000-0002-2468-3577>

Antonio Parodi  <https://orcid.org/0000-0002-8505-0634>

Giovanna Venuti  <https://orcid.org/0000-0003-0728-3763>

REFERENCES

- Benjamin, S.G., Grell, G.A., Brown, J.M. and Smirnova, T.G. (2004) Mesoscale weather prediction with the RUC hybrid isentropic-terrain-following coordinate model. *Monthly Weather Review*, 132, 473–494. [https://doi.org/10.1175/1520-0493\(2004\)132<0473:MWPWTF>2.0.CO;2](https://doi.org/10.1175/1520-0493(2004)132<0473:MWPWTF>2.0.CO;2).
- Blamey, R.C. and Reason, C.J.C. (2009) Numerical simulation of a mesoscale convective system over the east coast of South Africa. *Tellus*, 61A, 17–34. <https://doi.org/10.1111/j.1600-0870.2008.00366.x>.
- Ralph, R., Burton, A.G., Blyth, A.M. and Mobbs, S.D. (08 2013) Modelling isolated deep convection: a case study from COPS. *Meteorologische Zeitschrift*, 22(4), 433–443. <https://doi.org/10.1127/0941-2948/2013/0408>.
- Camberlin, P. and Philippon, N. (2002) The East African March–May rainy season: associated atmospheric dynamics and predictability over the 1968–97 period. *Journal of Climate*, 15(9), 1002–1019. [https://doi.org/10.1175/1520-0442\(2002\)015<1002:TEAMMR>2.0.CO;2](https://doi.org/10.1175/1520-0442(2002)015<1002:TEAMMR>2.0.CO;2).
- Camberlin, P., Fontaine, B., Louvet, S., Oettili, P. and Valimba, P. (2010) Climate adjustments over Africa accompanying the Indian monsoon onset. *Journal of Climate*, 23(8), 2047–2064. <https://doi.org/10.1175/2009JCLI3302.1>.
- Camberlin, P., Gitau, W., Kiladis, G., Bosire, E. and Pohl, B. (2019) Intraseasonal to interannual modulation of diurnal precipitation distribution over Eastern Africa. *Journal of Geophysical Research: Atmospheres*, 124, 11863–11886. <https://doi.org/10.1029/2019JD031167>.
- Chen, F. and Dudhia, J. (2001) Coupling an advanced land surface-hydrology model with the Penn State-NCAR MM5 modeling system. Part I: model implementation and sensitivity. *Monthly Weather Review*, 129, 569–585. [https://doi.org/10.1175/1520-0493\(2001\)129<0569:CAALSH>2.0.CO;2](https://doi.org/10.1175/1520-0493(2001)129<0569:CAALSH>2.0.CO;2).
- Crétat, J., Pohl, B., Richard, Y. and Drobinski, P. (2012) Uncertainties in simulating regional climate of Southern Africa: sensitivity to physical parameterizations using WRF. *Climate Dynamics*, 38, 613–634. <https://doi.org/10.1007/s00382-011-1055-8>.
- Crétat, J., Vizy, E.K. and Cook, K.H. (2014) How well are daily intense rainfall events captured by current climate models over Africa?. *Climate Dynamics*, 42, 2691–2711. <https://doi.org/10.1007/s00382-013-1796-7>.
- Davis, A.C., Brown, B. and Bullock, R. (2006a) Object-based verification of precipitation forecasts. Part I: methodology and application to mesoscale rain areas. *Monthly Weather Review*, 134, 1772–1784. <https://doi.org/10.1175/MWR3145.1>.
- Davis, A.C., Brown, B. and Bullock, R. (2006b) Object-based verification of precipitation forecasts. Part II: application to convective rain system. *Monthly Weather Review*, 134, 1785–1795. <https://doi.org/10.1175/MWR3146.1>.
- Dezfuli, A.K., Ichoku, C.M., Huffman, G.J., Mohr, K.I., Selker, J.S., van de Giesen, N., Hochreutener, R. and Annor, F.O. (2017a) Validation of IMERG precipitation in Africa. *Journal of Hydrometeorology*, 18, 2817–2825. <https://doi.org/10.1175/JHM-D-17-0139.1>.
- Dezfuli, A.K., Ichoku, C.M., Mohr, K.I. and Huffman, G.J. (2017b) Precipitation characteristics in West and East Africa from satellite and in situ observations. *Journal of Hydrometeorology*, 18, 1799–1805. <https://doi.org/10.1175/JHM-D-17-0068.1>.
- Dudhia, J. (1989) Numerical study of convection observed during the Winter Monsoon Experiment using a mesoscale two-dimensional model. *Journal of the Atmospheric Sciences*, 46, 3077–3107. [https://doi.org/10.1175/1520-0469\(1989\)046<3077:NSOCOD>2.0.CO;2](https://doi.org/10.1175/1520-0469(1989)046<3077:NSOCOD>2.0.CO;2).
- Ebert, E.E. (2008) Fuzzy verification of high-resolution gridded forecasts: a review and proposed framework. *Meteorological Applications*, 15(1), 51–64. <https://doi.org/10.1002/met.25>.
- Favre, A., Hewitson, B., Lennard, C., Cerezo-Mota, R. and Tadross, M. (2013) Cut-off lows in the South Africa region and their contribution to precipitation. *Climate Dynamics*, 41, 2331–2351. <https://doi.org/10.1007/s00382-012-1579-6>.
- Finkensieper, S., Stengel, M., Selbach, N., Hollmann, R., Werscheck, M. and Meirink, J.F. (2018). Available at: https://wui.cmsaf.eu/safira/action/viewICDRDetails?acronym=CLAAS_V002_ICDR.
- Finkensieper, S., Meirink, J.F., van Zadelhoff, G.-J., Hanschmann, T., Benas, N., Stengel, M., Fuchs, P., Hollmann, R., Kaiser, J. and Werscheck, M. (2020) *CLAAS-2.1: CM SAF CLOUD property dAtAset using SEVIRI - Edition 2.1*. Satellite Application Facility on Climate Monitoring.
- Finney, D.L., Marsham, J.H., Walker, D.P., Birch, C.E., Woodhams, B.J., Jackson, L.S. and Hardy, S. (2019) The effect of westerlies on East African rainfall and the associated role of tropical cyclones and the Madden-Julian Oscillation. *Quarterly Journal of the Royal Meteorological Society*, 146, 647–664. <https://doi.org/10.1002/qj.3698>.
- Flaounas, E., Bastin, S. and Janicot, S. (2011) Regional climate modelling of the 2006 West African monsoon: sensitivity to convection and planetary boundary layer parameterisation using WRF. *Climate Dynamics*, 36, 1083–1105. <https://doi.org/10.1007/s00382-010-0785-3>.
- Gilliam, R.C. and Pleim, J.E. (2010) Performance assessment of new land-surface and planetary boundary layer physics in the WRF-ARW. *Journal of Applied Meteorology and Climatology*, 49(4), 760–774. <https://doi.org/10.1175/2009JAMC2126.1>.
- Grell, G.A. and Dévényi, D. (2002) A generalized approach to parameterizing convection combining ensemble and data assimilation techniques. *Geophysical Research Letters*, 29(14). <https://doi.org/10.1029/2002GL015311>.

- Hart, N.C.G., Reason, C.J.C. and Fauchereau, N. (2010) Tropical-extratropical interactions over southern Africa: three cases of heavy summer season rainfall. *Monthly Weather Review*, 138, 2608–2623. <https://doi.org/10.1175/2010MWR3070.1>.
- Hersbach, H., Bell, B., Berrisford, P., Hirahara, S., Horányi, A., Muñoz-Sabater, J., Nicolas, J., Peubey, C., Radu, R., Schepers, D., Simmons, A., Soci, C., Abdalla, S., Abellan, X., Balsamo, G., Bechtold, P., Biavati, G., Bidlot, J., Bonavita, M., De Chiara, G. and et al. (2020) The ERA5 global reanalysis. *Quarterly Journal of the Royal Meteorological Society*, 146(730), 1999–2049. <https://doi.org/10.1002/qj.3803>.
- Hong, S.Y. and Lim, J.O.J. (2006) The WRF single moment 6-class microphysics scheme (WSM6). *Journal of the Korean Meteorological Society*, 42, 129–151.
- Hong, S.Y., Noh, Y. and Dudhia, J. (2006) A new vertical diffusion package with an explicit treatment of entrainment processes. *Monthly Weather Review*, 134, 2318–2341. <https://doi.org/10.1175/MWR3199.1>.
- Huffman, G.J., Bolvin, D.T., Nelkin, E.J., Wolff, D.B., Adler, R.F., Gu, G., Hong, Y., Bowman, K.P. and Stocker, E.F. (2007) The TRMM multisatellite precipitation analysis (TMPA): Quasi-global, multiyear, combined-sensor precipitation estimates at fine scales. *Journal of Hydrometeorology*, 8(1), 38–55. <https://doi.org/10.1175/JHM560.1>.
- Huffman, G.J., Stocker, E.F., Bolvin, D.T., Nelkin, E.J. and Tan, J. (2019) *GPM IMERG Final Precipitation L3 Half Hourly 0.1 degree x 0.1 degree V06*. Goddard Earth Sciences Data and Information Services Center (GES DISC).
- Iacono, M.J., Delamere, J.S., Mlawer, E.J., Shephard, M.W., Clough, S.A. and Collins, W.D. (2008) Radiative forcing by long-lived greenhouse gases: calculations with the AER radiative transfer models. *Journal of Geophysical Research*, 113, D13103. <https://doi.org/10.1029/2008JD009944>.
- Janjic, Z. (1994) The Step-Mountain Eta Coordinate Model: further developments of the convection, viscous sublayer, and turbulence closure schemes. *Monthly Weather Review*, 122, 927–945. [https://doi.org/10.1175/1520-0493\(1994\)122](https://doi.org/10.1175/1520-0493(1994)122).
- Jiménez, P.A., Dudhia, J., González-Rouco, J.F., Navarro, J., Montávez, J.P. and García-Bustamante, E. (2012) A revised scheme for the WRF surface layer formulation. *Monthly Weather Review*, 140, 898–918. <https://doi.org/10.1175/MWR-D-11-00056.1>.
- Joyce, R.J., Janowiak, J.E., Arkin, P.A. and Xie, P. (2004) CMORPH: a method that produces global precipitation estimates from passive microwave and infrared data at high spatial and temporal resolution. *Journal of Hydrometeorology*, 5, 487–503. [https://doi.org/10.1175/1525-7541\(2004\)005<0487:CAMTPG>2.0.CO;2](https://doi.org/10.1175/1525-7541(2004)005<0487:CAMTPG>2.0.CO;2).
- Kain, J.S. (2004) The Kain-Fritsch convective parameterization: an update. *Journal of Applied Meteorology*, 43, 170–181. [https://doi.org/10.1175/1520-0450\(2004\)043<0170:TKCPAU>2.0.CO;2](https://doi.org/10.1175/1520-0450(2004)043<0170:TKCPAU>2.0.CO;2).
- Keat, W.J., Stein, T.H.M., Phaduli, E., Landman, S., Becker, E., Bopape, M.-J.M., Hanley, K.E., Lean, H.W. and Webster, S. (2019) Convective initiation and storm life cycles in convection-permitting simulations of the Met Office Unified Model over South Africa. *Quarterly Journal of the Royal Meteorological Society*, 145, 1323–1336. <https://doi.org/10.1002/qj.3487>.
- Kouadio, K., Bastin, S., Konare, A. and Ajayi, V.O. (2018) Does convection-permitting simulate better rainfall distribution and extreme over Guinean coast and surroundings?. *Climate Dynamics*. <https://doi.org/10.1007/s00382-018-4308-y>.
- Laprise, R., Hernández-Díaz, L., Tete, K., Sushama, L., Separović, L., Martynov, A., Winger, K. and Valin, M. (2013) Climate projections over cordex africa domain using the fifth-generation canadian regional climate model (crcm5). *Climate Dynamics*, 41, 3219–3246. <https://doi.org/10.1007/s00382-012-1651-2>.
- Le Coz, C. and van de Giesen, N. (2020) Comparison of rainfall products over Sub-Saharan Africa. *Journal of Hydrometeorology*, 21, 553–596. <https://doi.org/10.1175/JHM-D-18-0256.1>.
- Ma, L.-M. and Tan, Z.-M. (2009) Improving the behavior of the cumulus parameterization for tropical cyclone prediction: convection trigger. *Atmospheric Research*, 92, 190–211. <https://doi.org/10.1016/j.atmosres.2008.09.022>.
- Maisha, T.R. (2014). *textitThe influence of topography and model grid resolution on extreme weather forecasts over South Africa*. Master's thesis, Pretoria, University of Pretoria.
- Malherbe, J., Engelbrecht, F. and Landman, W. (2012) Projected changes in tropical cyclone climatology and landfall in the South-west Indian Ocean region under enhanced anthropogenic forcing. *Climate Dynamics*, 40, 2867–2886. <https://doi.org/10.1007/s00382-012-1635-2>.
- Manatsa, D., Morioka, Y., Behera, S.K., Matarira, C.H. and Yamagata, T. (2014) Impact of Mascarene high variability on the East African 'short rains'. *Climate Dynamics*, 42, 1259–1274. <https://doi.org/10.1007/s00382-013-1848-z>.
- Maranan, M., Fink, A.H. and Knippertz, P. (2018) Rainfall types over southern West Africa: objective identification, climatology and synoptic environment. *Quarterly Journal of the Royal Meteorological Society*, 144, 1628–1648. <https://doi.org/10.1002/qj.3345>.
- Meynadier, R., de Coëtlogon, G., Bastin, S., Eymard, L. and Janicot, S. (2015) Sensitivity testing of WRF parameterizations on air-sea interaction and its impact on water cycle in the Gulf of Guinea. *Quarterly Journal of the Royal Meteorological Society*, 141, 1804–1820. <https://doi.org/10.1002/qj.2483>.
- Mlawer, E., Steven, J., Taubman, J., Brown, P.D., Iacono, M.J. and Clough, S.A. (1997) Radiative transfer for inhomogenous atmospheres: RRTM, a validated correlated-k model for the longwave. *Journal of Geophysical Research*, 102, 16663–16682.
- Morrison, H., Thompson, G. and Tatarskii, V. (2009) Impact of cloud microphysics on the development of trailing stratiform precipitation in a simulated squall line: comparison of one- and two-moment schemes. *Monthly Weather Review*, 137, 991–1007. <https://doi.org/10.1175/2008MWR2556.1>.
- Nakanishi, M. and Niino, H. (2006) An improved Mellor-Yamada level 3 model: its numerical stability and application to a regional prediction of advecting fog. *Boundary-Layer Meteorology*, 119, 397–407. <https://doi.org/10.1007/s10546-005-9030-8>.
- Ndarana, T., Bopape, M.-J., Waugh, D. and Dyson, L. (2018) The influence of the lower stratosphere on ridging Atlantic ocean anticyclones over South Africa. *Journal of Climate*, 31, 6175–6187. <https://doi.org/10.1175/JCLI-D-17-0832.1>.
- Ndarana, T., Mpati, S., Bopape, M.-J., Engelbrecht, F. and Chikoore, H. (2020a) The flow and moisture fluxes associated with ridging South Atlantic Ocean anticyclones during the subtropical southern African summer. *International Journal of Climatology*, 1–18. <https://doi.org/10.1002/joc.6745>.
- Ndarana, T., Rammopo, T., Chikoore, H., Barnes, M. and Bopape, M.-J. (2020b) A quasi-geostrophic diagnosis of the zonal flow

- associated with cut-off lows over South Africa and surrounding oceans. *Climate Dynamics*, 55, 2631–2644. <https://doi.org/10.1007/s00382-020-05401-4>.
- Nicholson, S.E. (2016) The Turkana low-level jet: mean climatology and association with regional aridity. *International Journal of Climatology*, 36, 2598–2614. <https://doi.org/10.1002/joc.4515>.
- Nicholson, S.E. (2017) Climate and climatic variability of rainfall over eastern Africa. *Reviews of Geophysics*, 55, 590–635. <https://doi.org/10.1002/2016RG000544>.
- Nicholson, S.E. (2018) The ITCZ and the seasonal cycle over equatorial Africa. *Bulletin of the American Meteorological Society*, 99, 337–348. <https://doi.org/10.1175/BAMS-D-16-0287.1>.
- NOAA (2001). Available at: <http://www.emc.ncep.noaa.gov/mmb/mmbpll/eta12tpb/>.
- Noble, E., Druyan, L.M. and Fulakeza, M. (2014) The sensitivity of WRF daily summertime simulations over West Africa to alternative parameterizations. Part I: African wave circulation. *Monthly Weather Review*, 142, 1588–1608. <https://doi.org/10.1175/MWR-D-13-00194.1>.
- Noble, E., Druyan, L.M. and Fulakeza, M. (2017) The sensitivity of WRF daily summertime simulations over West Africa to alternative parameterizations. Part II: precipitation. *Monthly Weather Review*, 145, 215–233. <https://doi.org/10.1175/MWR-D-15-0294.1>.
- Otieno, G., Mutemi, J.N., Opijah, F.J., Ogallo, L.A. and Omondi, M.H. (2020) The sensitivity of rainfall characteristics to cumulus parameterization schemes from a WRF model. Part I: a case study over East Africa during wet years. *Pure and Applied Geophysics*, 177, 1095–1110. <https://doi.org/10.1007/s00024-019-02293-2>.
- Pleim, J.E. (2007) A combined local and nonlocal closure model for the atmospheric boundary layer. Part I: model description and testing. *Journal of Applied Meteorology and Climatology*, 46, 1383–1395. <https://doi.org/10.1175/JAM2539.1>.
- Pohl, B., Cr  tat, J. and Camberlin, P. (2011) Testing WRF capability in simulating the atmospheric water cycle over Equatorial East Africa. *Climate Dynamics*, 37, 1357–1379. <https://doi.org/10.1007/s00382-011-1024-2>.
- Rapolaki, R.S., Blamey, R.C., Hermes, J.C. and Reason, C.J.C. (2019) A classification of synoptic weather patterns linked to extreme rainfall over the Limpopo River Basin in southern Africa. *Climate Dynamics*, 53, 2265–2279. <https://doi.org/10.1007/s00382-019-04829-7>.
- Roberts, M.J., Vidale, P.L., Senior, C., Hewitt, H.T., Bates, C., Berthou, S., Chang, P., Christensen, H.M., Danilov, S., Demory, M.-E., Griffies, S.M., Haarsma, R., Jung, T., Martin, G., Minobe, S., Ringer, T., Satoh, M., Schiemann, R., Scoccimarro, E., Stephens, G. and Wehner, M.F. (2018) The benefits of global high resolution for climate simulation. *Bulletin of the American Meteorological Society*, 99, 2341–2359. <https://doi.org/10.1175/BAMS-D-15-00320.1>.
- Singleton, A.T. and Reason, C.J.C. (2006) Numerical simulations of a severe rainfall event over the Eastern Cape coast of South Africa: sensitivity to sea surface temperature and topography. *Tellus*, 58A, 355–367. <https://doi.org/10.1111/j.1600-0870.2006.00180.x>.
- Singleton, A.T. and Reason, C.J.C. (2007) A numerical model study of an intense cutoff low pressure system over South Africa. *Monthly Weather Review*, 135, 1128–1150. <https://doi.org/10.1175/MWR3311.1>.
- Skamarock, W.C., Klemp, J.B., Dudhia, J., Gill, D.O., Liu, Z., Berner, J., Wang, W., Powers, J.G., Duda, M.G., Barker, D.M. and Huang, X.-Y. (2019) *A Description of the Advanced Research WRF Version 4*, (p. 145). NCAR Technical Note NCAR/TN-556+STR. Boulder, CO: NCAR/UCAR.
- Sun, X., Xie, L., Semazzi, F. and Liu, B. (2015) Effect of lake surface temperature on the spatial distribution and intensity of the precipitation over the Lake Victoria basin. *Monthly Weather Review*, 143, 1179–1192. <https://doi.org/10.1175/MWR-D-14-00049.1>.
- Thompson, G. and Eidhammer, T. (2014) A study of aerosol impacts on clouds and precipitation development in a large winter cyclone. *Journal of the Atmospheric Sciences*, 71(10), 3636–3658. <https://doi.org/10.1175/JAS-D-13-0305.1>.
- Thompson, G., Field, P.R., Rasmussen, R.M. and Hall, W.D. (2008) Explicit forecasts of winter precipitation using an improved bulk microphysics scheme. Part II: implementation of a new snow parameterization. *Monthly Weather Review*, 136, 5095–5115. <https://doi.org/10.1175/2008MWR2387.1>.
- van de Giesen, N., Hut, R. and Selker, J.S. (2014) The Trans-African Hydro-Meteorological Observatory (TAHMO). *Wiley Interdisciplinary Reviews: Water*, 1, 341–348. <https://doi.org/10.1002/wat2.1034>.
- Vogel, P., Knippertz, P., Fink, A.H., Schlueter, A. and Gneiting, T. (2018) Skill of global raw and postprocessed ensemble predictions of rainfall over northern tropical Africa. *Weather and Forecasting*, 33, 369–388. <https://doi.org/10.1175/WAF-D-17-0127.1>.
- Wang, W. (2017) *WRF: More Runtime Options*. Sydney: WRF Tutorial. Available at: https://www.climate-science.org.au/sites/default/files/WRF_options.pdf.
- Wheeler, M.C. and Hendon, H.H. (2004) An all-season real-time multivariate MJO index: development of an index for monitoring and prediction. *Monthly Weather Review*, 132, 1917–1932.
- Zhang, C. and Wang, Y. (2017) Projected future changes of tropical cyclone activity over the western north and south Pacific in a 20-km-mesh regional climate model. *Journal of Climate*, 30, 5923–5941. <https://doi.org/10.1175/JCLI-D-16-0597.1>.

How to cite this article: Meroni AN, Oundo KA, Muita R, *et al.* Sensitivity of some African heavy rainfall events to microphysics and planetary boundary layer schemes: Impacts on localised storms. *Q.J.R. Meteorol. Soc.* 2021;147:2448–2468. <https://doi.org/10.1002/qj.4033>